

# The anatomy of the NGC 5044 group – II. Stellar populations and star-formation histories

J. Trevor Mendel<sup>1\*</sup>, Robert N. Proctor<sup>1</sup>, Jesper Rasmussen<sup>2</sup>, Sarah Brough<sup>1</sup>,  
Duncan A. Forbes<sup>1</sup>

<sup>1</sup>Centre for Astrophysics & Supercomputing, Swinburne University, Mail H39, Hawthorn, VIC 3122, Australia

<sup>2</sup>Observatories of the Carnegie Institution (Chandra Fellow), 813 Santa Barbara Street, Pasadena, CA 91101, USA

5 November 2018

## ABSTRACT

The distribution of galaxy properties in groups and clusters holds important information on galaxy evolution and growth of structure in the Universe. While clusters have received appreciable attention in this regard, the role of groups as fundamental to formation of the present day galaxy population has remained relatively unaddressed. Here we present stellar ages, metallicities and  $\alpha$ -element abundances derived using Lick indices for 67 spectroscopically confirmed members of the NGC 5044 galaxy group with the aim of shedding light on galaxy evolution in the context of the group environment.

We find that galaxies in the NGC 5044 group show evidence for a strong relationship between stellar mass and metallicity, consistent with their counterparts in both higher and lower mass groups and clusters. Galaxies show no clear trend of age or  $\alpha$ -element abundance with mass, but these data form a tight sequence when fit simultaneously in age, metallicity and stellar mass. In the context of the group environment, our data support the tidal disruption of low-mass galaxies at small group-centric radii, as evident from an apparent lack of galaxies below  $\sim 10^9 M_\odot$  within  $\sim 100$  kpc of the brightest group galaxy. Using a joint analysis of absorption- and emission-line metallicities, we are able to show that the star-forming galaxy population in the NGC 5044 group appears to require gas removal to explain the  $\sim 1.5$  dex offset between absorption- and emission-line metallicities observed in some cases. A comparison with other stellar population properties suggests that this gas removal is dominated by galaxy interactions with the hot intragroup medium.

**Key words:** galaxies: clusters: NGC 5044 group - galaxies: distances and redshift - galaxies: fundamental parameters - galaxies: formation - galaxies: evolution

## 1 INTRODUCTION

Large photometric surveys have established that the observable galaxy population forms two distinct sequences in colour-magnitude space: a red sequence of predominantly early-type galaxies and a star-forming, late-type dominated blue sequence (e.g. Hogg et al. 2002; Blanton et al. 2003; Baldry et al. 2006). Recent observational evidence suggests that growth of the red sequence since  $z \sim 1$  is dominated by increasing numbers of low-luminosity ( $\lesssim L^*$ ) red galaxies with cosmic time at the expense of the low-luminosity star-forming galaxy population (e.g. Bell et al. 2004; Bundy et al. 2006; Brown et al. 2007; Faber et al. 2007). Hence, our

understanding of growth and evolution in the red sequence is closely related to our knowledge of processes responsible for quenching star formation in blue-sequence galaxies, enabling their subsequent evolution onto the red sequence.

The dichotomy of observed galaxy colours carries with it an increasingly well-described environmental dependence whereby galaxies inhabiting high-density regions are on average redder, older, more concentrated and more massive than galaxies found in the field (e.g. Oemler 1974; Dressler 1980; Goto et al. 2003; Blanton 2005; Blanton & Berlind 2007; O’Mill, Padilla & Lambas 2008; Cooper et al. 2008). This strong correlation of red-sequence galaxies with local galaxy density has led to a significant body of work devoted to exploring the environmental factors responsible for creating these predominantly red populations from the blue, star-

\* tmendel@swin.edu.au

forming population of field galaxies. Of the possible mechanisms for suppressing star formation, ram-pressure stripping (e.g. Gunn & Gott 1972; Hester 2006), mergers (e.g. Toomre & Toomre 1972; Negroponte & White 1983; Somerville & Primack 1999; McIntosh et al. 2008), strangulation (e.g. Larson, Tinsley & Caldwell 1980; Balogh & Morris 2000), tidal interactions and harassment (e.g. Farouki & Shapiro 1981; Moore et al. 1996) are the most frequently invoked to account for the increasing number density of red galaxies. Identifying *which* of these possible processes represents the dominant evolutionary path, however, remains an active field of research.

The Sloan Digital Sky Survey (SDSS) has proved fundamental in exploring the environmental dependence of galaxy properties, and has been used to show that the transformation of galaxies from blue to red takes place over relatively long timescales,  $\gtrsim 1$  Gyr, through the slow exhaustion of gas available for star formation, rather than rapid, violent removal (e.g. Kauffmann et al. 2004; van den Bosch et al. 2008). The dominance of so called “strangulation” (Balogh & Morris 2000) precludes cluster-cores as dominant sites for blue galaxy transformation as disruption processes in high-density regions, e.g. ram-pressure stripping and harassment, act over relatively short timescales (e.g. Abadi, Moore & Bower 1999; Quilis, Moore & Bower 2000). This supports earlier work from the 2dF Galaxy Redshift Survey (2dFGRS) which found that the fraction of star forming galaxies is lower with respect to the field even at the relatively low surface densities of loose groups,  $\sim 1\text{--}2$  galaxies/Mpc<sup>2</sup>, i.e. well outside dense cluster cores (e.g. Lewis et al. 2002; Poggianti et al. 2006).

While the majority of our understanding of the variation of galaxy properties with environment hinges on large photometric surveys, an alternative approach is the use of spectral absorption features as detailed tracers of galaxy stellar populations. In many ways spectral analyses provide a vastly increased level of detail for determining paths of galaxy formation and evolution relative to photometry, but they are often hindered by smaller sample sizes and relatively high observational expense. Nevertheless, absorption-line studies have met with great success in tracing the stellar populations of individual galaxies (e.g. Proctor et al. 2004; Thomas et al. 2005; Sánchez-Blázquez et al. 2006; Peletier et al. 2007; Spolaor et al. 2008), clusters (e.g. Smith, Lucey & Hudson 2007; Smith et al. 2008a,b; Trager et al. 2008) and large survey samples (e.g. Gallazzi et al. 2006; Jimenez et al. 2007; Proctor et al. 2008).

To date, spectroscopic studies with a particular focus on environment have primarily made use of cluster galaxy populations. Caldwell, Rose & Concannon (2003) used a sample of nearby early-type galaxies in the Virgo Cluster, as well as a field-galaxy sample, to probe galaxy stellar populations to low masses (stellar velocity dispersions,  $\sigma, < 100$  km s<sup>-1</sup>). Caldwell et al. (2003) found a greater intrinsic scatter in the properties of low-mass galaxies, but made no particular effort to examine the spatial distribution of galaxy populations within the Virgo Cluster. In similar work, Smith et al. (2007) and Smith et al. (2008a,b) have examined the stellar populations of dwarf galaxies in the Coma Cluster and Shapley supercluster, in both instances finding that the scaling relations of low-mass populations are generally consistent with the relations of higher-mass

E and S0 galaxies, although with the same increased scatter noted by Caldwell et al. (2003). In the case of Coma, Smith et al. (2008a) find a radial dependence of both age and metallicity, where galaxies at larger projected radii are both younger and higher metallicity, suggestive of recently quenched star formation among galaxies entering the Coma cluster outskirts and consistent with earlier spectral studies of Coma cluster galaxies (Caldwell et al. 1993; Mobasher et al. 2001; Carter et al. 2002).

These studies, however, only serve to probe rare high-density cluster environments, neglecting the much more common group environment. In an attempt to fill this gap, here we undertake a detailed spectroscopic study of the galaxy population in the NGC 5044 group with the aim of describing galaxy evolutionary histories and reconstructing the formation history of the group as a whole. In a previous paper (Mendel et al. 2008; hereafter Paper I), we used new, deep spectroscopic observations in conjunction with archival velocity information to more than triple the number of velocity-confirmed group members. This greatly improved sample has allowed us to characterise the dynamical state of the group, which we find to be relaxed from a combination of X-ray and dynamical indicators. Here, we turn our focus to analysing the stellar populations of galaxies in this redefined group with a focus on establishing the details of galaxy evolution in the context of the group environment.

The structure of this paper is as follows: Section 2 describes the spectroscopic data used from both new AAOmega observations and the 6dF Galaxy Survey. Here we also describe the method used to derive kinematic properties. In Section 3 we discuss the measurement of Lick index absorption features and their interpretation in terms of age, metallicity and  $\alpha$ -element abundance (Section 4). In subsequent sections we discuss the stellar population properties of NGC 5044 group galaxies both as an independent galaxy sample (Section 5), and in the context of their place in the group as a whole (Section 6). In Section 7 we describe the distribution of emission-line properties for NGC 5044 group galaxies. In Section 8 we discuss our stellar population findings in relation to the dynamical description of the group presented in Paper I, as well as their relevance to the formation and evolution of the NGC 5044 group and galaxies therein.

Throughout this paper we assume  $H_0 = 70$  km s<sup>-1</sup> Mpc<sup>-1</sup> where relevant. We adopt a distance modulus for the NGC 5044 group of  $(m - M)_0 = 32.31$  (28.99 Mpc) measured using surface brightness fluctuations (Tonry et al. 2001) with corrections applied to adjust for the improved Cepheid distance measurements of Jensen et al. (2003). Where specified, correlations have been measured using the Kendall rank-order correlation test with significance quoted from the two-tailed p-value.

## 2 DATA

Here we use the NGC 5044 group sample defined in Paper I, which consists of 111 spectroscopically-confirmed group members compiled using newly obtained redshifts from AAOmega supplemented using the 6dF Galaxy Survey Data

Release 2 (6dFGS DR2<sup>1</sup>; Jones et al. 2005), HI observations (Kilborn et al. in preparation) and the Nasa/IPAC Extragalactic Database (NED) sources. Of these 111 galaxies, 95 have spectra available from AAOmega and 6dFGS observations which can be used to measure absorption indices (71 from our new AAOmega observations and 24 from 6dFGS DR2). These spectral data are summarised below.

## 2.1 AAOmega spectroscopy

New observations of NGC 5044 group galaxies were carried out using the AAOmega multi-object spectrograph on the 3.9m Anglo-Australian Telescope (AAT) in Siding Spring, Australia. Target galaxies were taken from the list of potential NGC 5044 group members of Ferguson & Sandage (1990). Medium resolution 580V and 385R gratings were used, yielding FWHM dispersions of 3.5 Å and 5.3 Å for blue ( $\lambda\lambda 3700\text{--}5700\text{Å}$ ) and red ( $\lambda\lambda 5700\text{--}8800\text{Å}$ ) spectra respectively.

Galaxies were separated into high- and low-luminosity subsamples using an apparent magnitude cut of  $B = 15$  and observed separately in order to limit the effects of scattered light from the brightest sources. Observations were carried out 30 minutes at a time with a total of 3 to 4 observations per plate configuration. In addition to fibres assigned to galaxies, in each configuration an additional 30 to 35 “empty” fibres were assigned to be used for sky subtraction. There are several relatively wide defects in the blue arm CCD of AAOmega, and to limit the effects of these on our final coadded science spectra we offset the central wavelength on each night of observations by 100 Å, ensuring that usable data were obtained from at least two out of three nights at every wavelength. Our total integration time for high- and low-luminosity galaxies was 4 and 17 hours respectively.

In addition to our primary (galaxy) targets we have observed a set of calibration stars. These include stars common to the Lick stellar library (see §3.2) and a set of spectrophotometric calibrators which we can use to roughly flux calibrate the AAOmega data.

Data were reduced using a combination of IRAF routines and the 2DFDR reduction pipeline supplied and maintained by the Anglo-Australian Observatory. Prior to reduction with 2DFDR an average bias was subtracted from all frames and bad pixel columns were identified and repaired. We then used 2DFDR to reject cosmic rays, identify fibre apertures, flat-field, throughput calibrate and sky subtract the data. The final coaddition of science frames was carried out after excluding any single exposures with very low flux relative to the other frames.

In this work, we consider only those galaxies identified as group members in Paper I, and refer the reader to that work for the details of how group membership was defined. We exclude from subsequent analyses any galaxies with a signal-to-noise (S/N) of less than 12, as below this we consider stellar population measurements to be highly unreliable. This cut excludes 19 galaxies, leaving a total of 52 from the original AAOmega sample described in Paper I.

## 2.2 6dFGS Spectral Data

The 6dFGS covers 17046 deg<sup>2</sup> of the Southern sky using the Six-Degree Field (6dF) multi-fibre spectrograph on the UK Schmidt Telescope. The survey targets are selected from the 2MASS Extended Source Catalogue (2MASS XSC; Jarrett et al. 2000), 2MASS and SuperCOSMOS to include all galaxies brighter than  $K_{\text{tot}} = 12.75$  mag with wavelength coverage from  $\lambda\lambda 4000\text{--}8400\text{Å}$ . In Paper I we include 16 unique 6dFGS galaxies and 8 galaxies that overlap with our AAOmega sample, all of which have spectra available. However, applying a similar cut in S/N as the AAOmega data above excludes an additional 9 of the 6dFGS galaxies, leaving a total of 15 for stellar populations analysis.

The combined AAOmega and 6dFGS sample then consists of 67 confirmed group-member galaxies with  $S/N > 12$ , which we use for the remainder of this analysis.

## 2.3 Recession velocity and velocity dispersion measurements

Recession velocities and velocity dispersions were fit simultaneously using the penalised pixel-fitting (pPXF) software of Cappellari & Emsellem (2004). Pixel fitting methods are notoriously sensitive to the templates used, so it is important to minimise the effects of so-called template mismatch on kinematic measurements. The pPXF code is an extension of the Gauss-Hermite fitting method of van der Marel & Franx (1993) which allows for fitting to be carried out using a linear combination of template spectra, all but eliminating template-mismatch-induced errors.

As our input templates we use 50 stellar spectra from the MILES standard star library (Sánchez-Blázquez et al. 2006) spanning a broad range of spectral types. The particular choice of stars used to construct templates has only a minimal effect on the results derived using pPXF as long as they span a similar range of spectral types. We have investigated this briefly by fitting a sub-sample of our galaxy data with sets of 50 randomly chosen stars from the MILES library and find typical deviations of  $\sim 4\text{--}5$  km s<sup>-1</sup> in velocity dispersion.

In order for pPXF to provide meaningful velocity dispersion outputs we need to account for the difference in instrumental dispersion between our AAOmega spectra and the MILES stellar library. Overlap between the Lick and MILES stellar libraries is significant, so we have used the Lick standard stars observed throughout our AAOmega observing run to effectively measure the wavelength dependent broadening offset between AAOmega and the MILES library. In total we use 5 Lick/MILES stars to measure the median broadening difference. We find that scatter in our broadening measurements is significant for wavelengths below 4700 Å, but above this wavelength the dispersion offset is relatively stable at  $\sim 57.7$  km s<sup>-1</sup> (2.3 Å FWHM). Adding in quadrature the spectral resolution of the MILES library, 2.3 Å, gives an average spectral resolution for AAOmega between 4700 Å and 5400 Å of 3.2 Å FWHM. This derived resolution is consistent with that found by Smith et al. (2007) for spectra taken using the 580V grating on AAOmega.

Standard star observations for the 16 6dFGS galaxies that we define as group members are unavailable, but we can measure the broadening offset between AAOmega

<sup>1</sup> The most recent data release available at the time of writing.

and 6dF using the 8 galaxies present in both samples. In the  $\lambda\lambda 4700\text{--}5400\text{ \AA}$  wavelength range we find a mean offset between AAOmega and 6dFGS spectra of  $103.6\text{ km s}^{-1}$  ( $4.1\text{ \AA}$  FWHM). Adding in quadrature the previously measured offset between AAOmega and the MILES library in this spectral region we adopt a total broadening of  $118.6\text{ km s}^{-1}$  ( $4.7\text{ \AA}$  FWHM). The difference in aperture size between the 6dF and AAOmega fibres ( $6.7''$  vs.  $2.1''$ ) will result in an additional broadening difference between the two galaxy spectra, independent of instrument resolution, of order 5 percent (Jørgensen, Franx & Kjærgaard 1995). We do not take this aperture effect into account when calculating our broadening as the statistical nature of the Jørgensen et al. (1995) correction will likely only serve to introduce scatter in our relatively small number of galaxies, particularly given our broad range of galaxy types.

Prior to measuring kinematics using pPXF, MILES template spectra are smoothed to the AAOmega and 6dFGS resolution using the measured broadening offsets. The pPXF code allows for a penalty to be applied to the higher order terms of the Gauss-Hermite polynomials and here we adopt a moderately high bias of 0.8 throughout fitting in order to limit spurious results from undersampled or low S/N data. Random errors on our kinematic measurements are then calculated using a series of Monte Carlo simulations spanning a range of velocity dispersions and S/N. The scatter in our determination of instrumental broadening discussed above adds an additional, systematic uncertainty to our velocity dispersion measurements of  $22\text{ km s}^{-1}$  and  $41\text{ km s}^{-1}$  for AAOmega and 6dFGS galaxies respectively, which we include in quadrature.

## 2.4 Emission-line measurements

We identify emission-line galaxies through examination of residuals to the best fit pPXF templates, and for 24 galaxies in our sample we find evidence for emission in some combination of  $H\beta$ ,  $[\text{OIII}]_{\lambda 4959}$ ,  $[\text{OIII}]_{\lambda 5007}$ ,  $[\text{NI}]_{\lambda 5198}$  and  $[\text{NI}]_{\lambda 5200}$ . While we can estimate emission-line fluxes from the residuals of our template fits, the underlying absorption in these regions is generally poorly constrained as emission contaminated lines are masked in the template fitting process.

A far more robust method is to fit for absorption- and emission-line kinematics simultaneously, which we carry out using the GANDALF software of Sarzi et al. (2006). This is an extension of the pPXF pixel fitting routine described in §2.3 which fits simultaneously a set of absorption and emission templates, eliminating errors introduced by fitting emission line residuals separately. Fits to emission lines are conducted using a set of independent Gaussian profiles whose kinematics can be varied as required. Here we treat the kinematics of nebular and Balmer-line emission separately, tying each to the kinematics of the dominant features in appropriate regions of our spectra ( $H\beta$  or  $H\alpha$  and  $[\text{OIII}]_{\lambda 5007}$  or  $[\text{NII}]_{\lambda 6583}$  for Balmer and nebular lines respectively). Our choice to fit separately the kinematics of Balmer and nebular emission lines has a negligible effect on our results as we find no galaxies with a significant kinematic difference between the two (where both are detected). There is generally good agreement between kinematics measured using pPXF and GANDALF; the largest offsets are observed in velocity disper-

sion, and are only significant in galaxies with strong emission lines and relatively weak continuum flux.

GANDALF also allows for spectra to be cleaned of detected emission. Here we follow Sarzi et al. (2006) and adopt an amplitude-to-noise (A/N) threshold of 4, where noise is defined as the scatter about the best-fit absorption template. As both [NI] and  $H\beta$  emission strongly affect our Lick index measurements the removal of these lines results in a significant improvement in the quality of stellar population fits for emission-line galaxies (see discussion in Section 4). The approximate detection threshold of emission lines in our data can be calculated as a function of S/N using our adopted A/N and typical line broadening. If we assume a typical intrinsic line width of  $\sim 30\text{--}50\text{ km s}^{-1}$ , then our sensitivity is  $\sim 0.6\text{ \AA}$  for AAOmega data and  $\sim 0.9\text{ \AA}$  for 6dFGS data at the median S/N of our galaxy data.

We use the  $H\alpha/H\beta$  Balmer decrement to calculate the extinction correction for our emission-line fluxes where applicable using the  $R_V = 3.1$  reddening curve of Cardelli, Clayton & Mathis (1989) and an intrinsic  $H\alpha/H\beta$  line ratio of 2.85 (Osterbrock 1989). In galaxies with very low extinction the errors on our line-flux measurements can sometimes result in a negative extinction estimate. As this is clearly non-physical we adopt  $E(B-V) \leq 0.01$  as an upper limit of extinction and assign this to galaxies with low or spurious (i.e. negative) extinction measurements.

## 3 LICK INDEX MEASUREMENTS AND CALIBRATION TO THE LICK/IDS SYSTEM

Here we use Lick absorption features (Burstein et al. 1984; Trager et al. 1998) to characterise the stellar populations of our galaxies. Lick indices are defined based on their particular sensitivity to either age or metallicity, and so are useful for describing these parameters in integrated spectra. Lick line-strength measurements were carried out using the index definitions of Trager et al. (1998), supplemented with higher-order Balmer line definitions from Worthey & Ottaviani (1997). We omit from our Lick index measurements  $\text{Fe}5782$ ,  $\text{NaD}$ ,  $\text{TiO}_1$  and  $\text{TiO}_2$  as these fall in the wavelength range of the AAOmega dichroic where sensitivity is decreasing rapidly.

### 3.1 Velocity dispersion corrections

In order to properly compare measured indices with SSP models it is important that the total broadening of any given absorption feature matches the wavelength-dependent broadening of the Lick/IDS system. Galaxies with combined instrumental and velocity-dispersion broadening less than the target Lick resolution are broadened as necessary using a wavelength-dependent Gaussian kernel to match the description of the Lick/IDS resolution given by Worthey & Ottaviani (1997).

In cases where the combined instrument and velocity dispersion broadening is greater than the required Lick/IDS system resolution we calculate line-width corrections based on iteratively broadened template stars. These line-width adjustments are then applied to correct measured indices back to the desired Lick/IDS resolution. As a test of this method, Proctor & Sansom (2002) compare stellar and

**Table 1.** Lick index corrections for AAOmega data and their associated errors.

Index	Offset	$\sigma_{rms}$
H $\delta_A$	0.148	0.426
H $\delta_F$	0.053	0.208
CN <sub>1</sub>	0.018	0.008
CN <sub>2</sub>	0.024	0.010
Ca4227	0.153	0.098
G4300	-0.029	0.110
H $\gamma_A$	0.244	0.255
H $\gamma_F$	0.099	0.118
Fe4383	0.362	0.093
Ca4455	0.386	0.049
Fe4531	0.025	0.107
C4668	-0.569	0.197
H $\beta$	-0.133	0.039
Fe5015	0.222	0.074
Mg <sub>1</sub>	0.028	0.002
Mg <sub>2</sub>	0.036	0.002
Mgb	0.006	0.051
Fe5270	-0.096	0.125
Fe5335	-0.004	0.055
Fe5406	-0.014	0.039
Fe5709	0.183	0.090

galaxy spectra broadened using this technique, finding good agreement between the two. For further details see Proctor & Sansom (2002).

### 3.2 Lick/IDS system calibration

In order to calibrate index measurements to the Lick/IDS system, we have observed several stars from the Lick stellar library at the beginning of each night. Index measurements for AAOmega data are then adjusted based on a comparison of published Lick standard star indices and our stellar observations. The mean offsets found for each index are listed in Table 1, along with their associated r.m.s. error.

We are unable to calibrate 6dFGS data in the same way as AAOmega data, and so we generate two sets of indices for 6dFGS galaxies: the first using the corrections provided in Table 1, and the second with no correction. We refer the reader to §4.1 for a comparison of the properties derived using these two sets of indices for overlapping 6dFGS and AAOmega galaxies.

### 3.3 Index errors

The fitting technique that we adopt for these data involves the simultaneous  $\chi^2$  minimisation for a large number of Lick indices ( $\sim 20$ ). In order for these fits to be reliable, an accurate representation of index errors is crucial, but notoriously difficult to obtain for spectral observations.

Proctor et al. (2008; hereafter P+08) have recently used spectra from the 6dFGS DR1 (Jones et al. 2004) to measure ages and metallicities in a large sample of galaxies using Lick indices. In estimating their index errors, P+08 have used duplicate observations of the same galaxy (from overlapping survey regions) to calculate the r.m.s. scatter in their Lick index measurements at a given S/N. The r.m.s. value was then fit as a function of S/N using the form  $r.m.s. = a/(S/N + b)$ ,

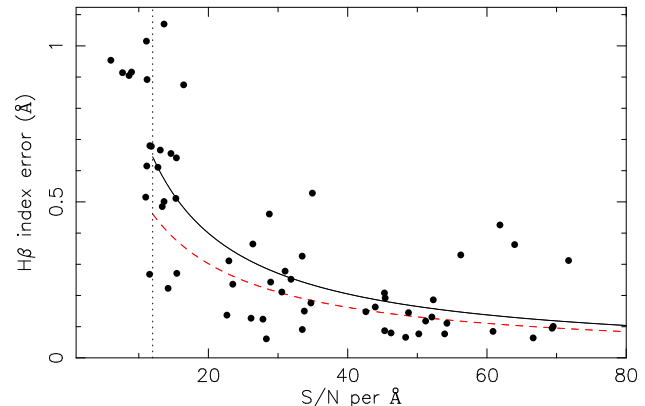


**Figure 1.** H $\beta$  index error vs. signal-to-noise for galaxies in our spectroscopic sample. The *solid* line shows the best fit to our measured index errors as a function of S/N (see §3.3), while the *dashed* line shows a similar fit for 6dFGS DR1 data derived by P+08. The *dotted*, vertical line shows our adopted S/N cut of 12.

where  $a$  and  $b$  are constants, which was then used to calculate representative errors for the rest of the galaxy sample based on their S/N. This method not only encapsulates redshift and velocity dispersion errors, but also errors resulting from sky subtraction, fibre flat-fielding and throughput calibration that are nearly impossible to quantify in individual fibre observations.

Here we adopt a similar strategy to P+08 and exploit the composite nature of our final spectra by re-measuring indices on individual observations, of which there are 12 and 34 observations each for bright and faint galaxies respectively. We then adopt the  $\sigma_{rms}$  for these repeat measurements as an accurate representation of the stochastic errors in our sample (i.e. Poisson noise, sky-subtraction etc). In Fig. 1 we show how the H $\beta$  index error derived in this manner varies as a function of S/N for the galaxies in our sample, and for comparison we also show the line describing index errors as derived by P+08 for 6dFGS DR1 data. Error curves for all indices are shown in Appendix A.

For our AAOmega data the total adopted index error is a combination of this random error, the  $\sigma_{r.m.s.}$  associated with conversion to the Lick/IDS system (§3.2) and the index broadening due to errors on velocity dispersion and recession velocity measurements (§2.3). For 6dFGS data we adopt the recession velocity and velocity dispersion errors as discussed in §2.3, as well as the index errors as a function of S/N derived by P+08.

## 4 STELLAR POPULATION MODELS AND FITTING

Having compiled relevant Lick index measurements and their corresponding error, we now turn to the task of interpreting these measurements in terms of the stellar population parameters they describe. Here we use the Single Stellar Population (SSP) models of Thomas, Maraston & Bender (2003) with account for variable abundance ratios as calculated by Korn, Maraston & Thomas (2005; hereafter we refer to the Thomas et al. 2003 and Korn et al. 2005 models collectively as TMB03). These models cover the metallicity range  $-2.25 \leq [Z/H] \leq 0.65$  with ages from 1 to 15 Gyrs. The

variable abundance ratios included by TMB03 consider N, O, Mg, Ca, Na, Si and Ti as enhanced elements and, while these fall outside a strict definition of  $\alpha$ -elements, we will hereafter refer to enhancement measures from the TMB03 models as  $\alpha$ -element abundances or  $[\alpha/\text{Fe}]$ .

It is well known that spectra are degenerate with respect to age and metallicity in so much as old, metal-rich and young, metal-poor stellar populations are remarkably similar. In order to minimise the influence of this degeneracy on our final measurements, we adopt the  $\chi^2$  minimisation technique of Proctor et al. (2004), simultaneously fitting as many Lick indices as possible. This method has been shown to recover reliable ages, metallicities and  $\alpha$ -element abundances in both galaxies (e.g. Proctor & Sansom 2002; Brough et al. 2007; Proctor et al. 2008) and globular clusters (Beasley et al. 2004; Pierce et al. 2006; Mendel et al. 2007).

Our goal is to obtain a stable fit between our galaxy data and the TMB03 models, and to accomplish this we adopt an iterative approach to our fitting. As a first step we perform a fit using as many indices as our data allow, generally between 18 and 21. In subsequent iterations indices deviant from the best-fit solution at the 5, 4 and 3  $\sigma$  levels are clipped. A final, manual inspection of the fit is then carried out to ensure that stable fits have been attained and that indices have not been over- or under-clipped as a result of poor error estimates.

Figs. 2 and 3 show the mean deviation of indices from the best fit model for AAOmega and 6dFGS data respectively. Galaxies free of emission are generally fit very well by the TMB03 models and we clip at most 2 indices from any given galaxy. Emission-line galaxies are significantly more difficult to fit, however the emission-cleaned spectra output from GANDALF result in a large improvement to the overall quality of fits for AAOmega data (Fig 2b,c) and slight improvement for 6dFGS data (Fig. 3b,c).

Final errors on our stellar population measurements are estimated using a Monte Carlo method which re-samples the best-fit model convolved with our observed index errors. These error estimates represent our best attempt to quantify the random error contribution to our measurements, however there is an additional systematic error present in the models themselves which we do not account for (see, e.g., Conroy, Gunn & White 2008).

The 6dFGS and AAOmega spectra used in this work can only be used to derive *luminosity-weighted* ages, metallicities and  $\alpha$ -element abundances. This is important to any subsequent analyses as these luminosity-weighted values are particularly affected by small centralised bursts of star formation and may not be representative of the global galaxy properties. In addition, because of aperture size differences between AAOmega and 6dF (2.1'' vs. 6.7''; 0.3 kpc vs. 0.9 kpc at the distance of NGC 5044) we expect some variation in the derived stellar population parameters due to both sampling differences and the presence of radial gradients, predominantly in metallicity. Final measurements of stellar population parameters (ages, metallicities etc.) and their associated errors for the 67 galaxies in our spectral sample are included in Appendix B.

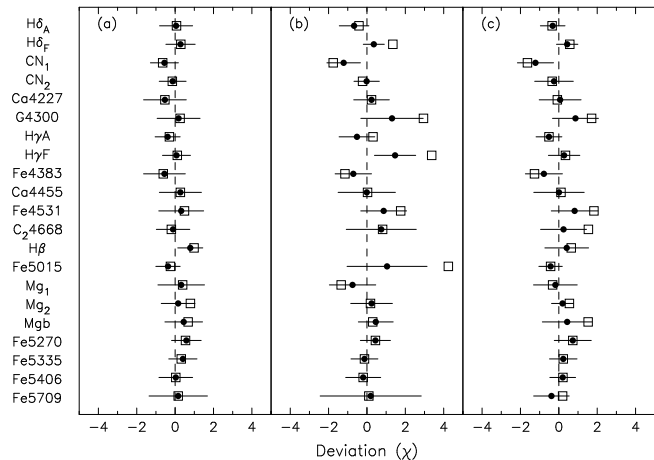


**Figure 2.** Mean deviation of indices from the best fit TMB03 SSP model. Open squares show the mean deviation for all indices in each galaxy, while filled circles show the mean deviation only for indices included in the fits. (a) Galaxies with no detectable emission, (b) galaxies with visible emission in their spectra and (c) emission galaxies with spectra cleaned using the GANDALF routine (see §2.4).

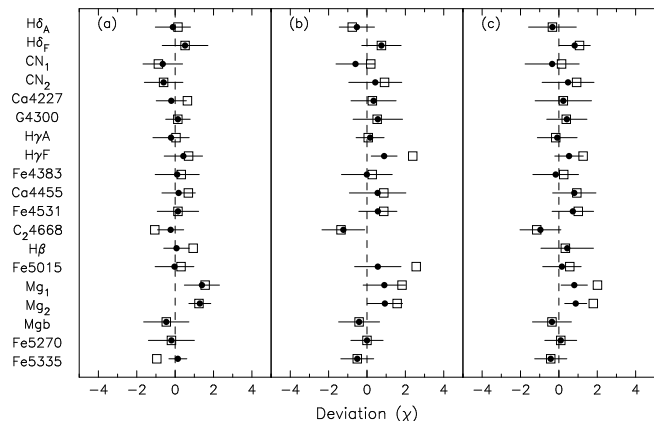


**Figure 3.** Same as Fig. 2, but for 6dFGS data. Data shown are without correction to the Lick/IDS system (see §4.1).

#### 4.1 Comparison of AAOmega and 6dFGS galaxies: agreement and aperture effects

In Fig. 4 we show the comparison of stellar population parameters derived for overlapping AAOmega and 6dFGS galaxies. In this comparison we have used indices measured from 6dFGS data with no Lick/IDS system correction applied. Using indices adjusted using the AAOmega Lick/IDS system correction gives similar results, but with an increase in scatter. We therefore use uncorrected 6dFGS indices for the remainder of this work.

Of particular interest here is the comparison between galaxy properties sampled using the different fibre apertures of AAOmega and 6dF. Perhaps the most obvious trend is observed in metallicity, which is also the most robust of our stellar population measurements. 6dFGS galaxies show a systematic offset towards lower metallicities of  $\sim 0.1$  dex, consistent with observations that the majority of galaxies possess negative gradients in metallicity (i.e. galaxies

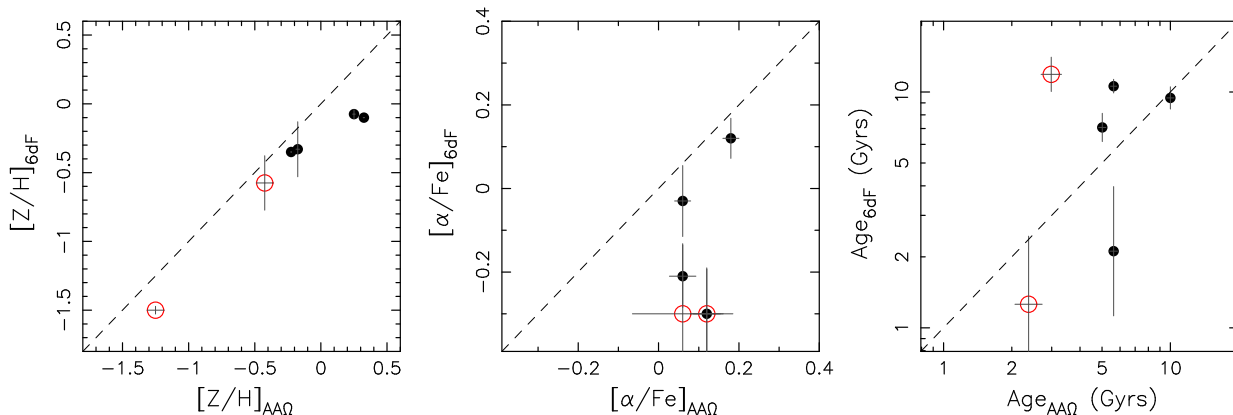


**Figure 4.** Comparison of metallicity ( $[Z/H]$ ),  $\alpha$ -element abundance and age for the 6 overlapping 6dFGS and AAOmega galaxies with  $S/N > 12$ . Open (red) and filled (black) circles represent galaxies with and without emission lines. *Dashed* lines in each panel represent equality. Parameters for 6dFGS data are shown with no applied correction to the Lick/IDS system (see §3.2).

are more metal-poor at larger radii, e.g. Sánchez-Blázquez et al. 2007; Brough et al. 2007).

Comparisons of  $\alpha$ -element abundances and ages are considerably more scattered than metallicity, indicative of the increased difficulty in their measurement. Broadly, we expect the larger fibre aperture of 6dF to yield older ages, particularly for galaxies with recent or currently ongoing star formation as these bursts are (generally) centrally concentrated. We find this to be the case for half of the 6dFGS galaxies, but the other half scatter to younger ages with considerable uncertainty. As these galaxies are just above our adopted  $S/N$  cut, we consider these measurements to be highly uncertain rather than representative of a real trend in the data. We expect the variation in aperture size between AAOmega and 6dF to have little systematic effect on the measured  $\alpha$ -element abundances, as observed gradients in  $[\alpha/Fe]$  are both weak and variable. In Fig. 4,  $\alpha$ -element measurements using AAOmega data are consistently higher than those from the 6dFGS data. Again, this is most likely a  $S/N$  effect as the small dynamic range of  $\alpha$ -element abundances makes their determination difficult in low  $S/N$  data.

Motivated by the comparisons in Fig. 4 and the discussion above, in forthcoming sections we consider galaxy metallicities to be robust for both the 6dFGS and AAOmega samples. Age and  $\alpha$ -element abundances for 6dFGS galaxies can be used to give a rough indicator of stellar population trends at larger group-centric radii (see §6.1 and Paper I), but we will refrain from using them to make any specific judgements due to the large uncertainty in their relationship to AAOmega data.

## 5 GALAXY PROPERTIES

### 5.1 Stellar population parameters versus stellar mass

Before attempting to place our observed galaxy population in the context of the NGC 5044 group environment, we first examine the properties of galaxies independent of their particular place in the group. In Fig. 5 we show how our measured ages, metallicities and  $\alpha$ -element abundance vary with stellar mass ( $M_*$ ). Stellar masses have been computed using

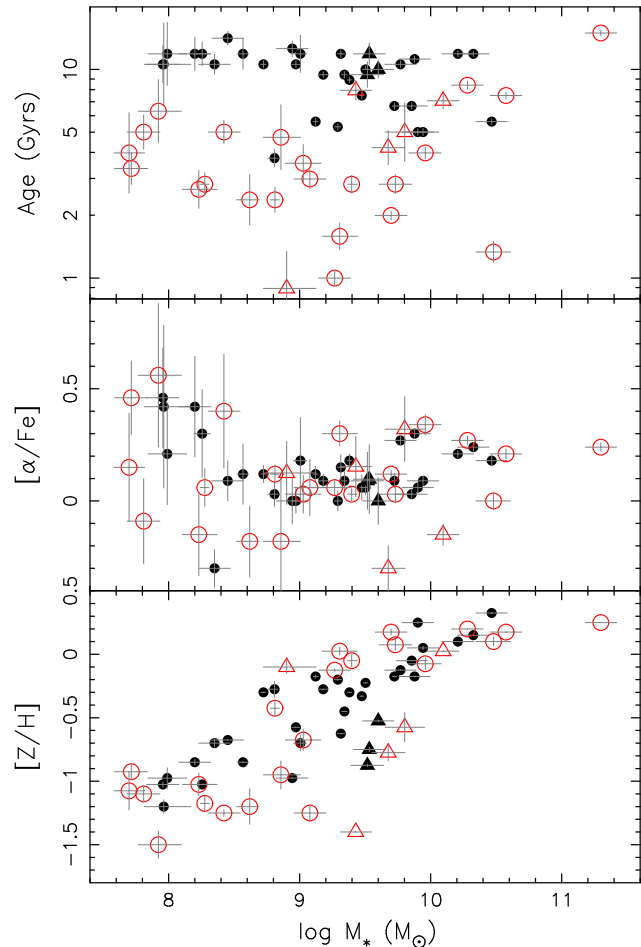


**Figure 5.** Relationship between stellar population properties and stellar mass (see §5.1). Filled (black) and open (red) symbols represent passive and emission-line galaxies (see §2.4), with circles and triangles delineating galaxies measured using AAOmega and 6dFGS spectra, respectively. Errors bars represent 1-sigma deviations estimated using the Monte Carlo technique described in Section 4.

GALEXEV stellar population synthesis models of Bruzual & Charlot (2003; hereafter BC03). Here we use BC03 models constructed using the “Padova 1994” isochrones (see BC03 and references therein) and stellar initial mass function (IMF) of Chabrier (2003). Using our derived central ages and metallicities, we then extract the appropriate  $B$ -band mass-to-light ratio (M/L) from the BC03 models.

Of the three stellar population parameters measured and shown in Fig. 5, metallicity shows the strongest correlation with mass, spanning more than two decades with a scatter of  $\sim 0.26$  dex. The general tightness of the mass-metallicity relation as determined from both emission- and absorption-line analyses is well known from large samples such as the SDSS (e.g. Tremonti et al. 2004; Gallazzi et al. 2006), however our data probe this relation an order of magnitude lower in both mass and metallicity. We see evidence for increased scatter among emission-line galaxies ( $\sim 0.39$  dex for emission-line galaxies vs.  $\sim 0.23$  dex for passive galaxies), which could be indicative of “contamination” from recently formed stellar populations, however the fact that metallicities for low-mass emission-line galaxies ( $\log M_* \lesssim 9$ ) appear depressed relative to their passive counterparts suggest that contamination is not playing a significant role, as recently formed populations should be metal-enriched. Instead, the observed low metallicities (as well as increased scatter) could be an effect of metal-enriched outflows in these galaxies, driven either by starbursts or supernovae, which could prevent the incorporation of metals into newly-formed stars. We note, however, that measurements for emission-line systems are also affected by the quality of our applied emission-line corrections, which would naturally lead to an increased scatter in absorption-line measurements in these systems.

An interesting question related to the mass-metallicity relation is the degree to which it depends on environment. While a detailed analysis of this dependence requires a comparison of galaxies at fixed stellar mass in a range of environments, even a qualitative comparison of the mass-metallicity relation in several different environments should allow identification of any gross systematic deviations. To this end, we have selected a comparative sample of galaxies, both at higher and lower masses, in two other environments, the Local Group and the Shapley supercluster. Data for Local Group dwarf galaxies are taken from the compilation of Woo, Courteau & Dekel (2008), who provide stellar masses, derived using the colour- $M_*/L$  relation of Bell & de Jong (2001), and average  $[Z/H]$  from red giant branch stars. Metallicities for a sample of galaxies in the Shapley supercluster have been calculated using Lick line index measurements from Smith et al. (2007) and the fitting methods described in Section 4. Stellar masses for these galaxies have been estimated as described above, using  $B$ -band magnitudes from Smith et al. (2007). A comparison of the mass-metallicity relation for these three samples is shown in Fig. 6. In this figure, metallicity estimates for Shapley supercluster galaxies have had additional offset of  $+0.15$  dex applied to account for the different physical aperture size between NGC 5044 and Shapley observations (0.3 kpc vs. 1.9 kpc re-

spectively)<sup>2</sup>. Data shown in Fig. 6 form a remarkably uniform mass-metallicity sequence over roughly six orders of magnitude in galaxy stellar mass, despite the widely varied environments sampled. Furthermore, apart from the obvious differences in stellar mass range, the data suggest that environment is likely playing only a small role in establishing the mass-metallicity relation, consistent with recent results from the SDSS (e.g. Mouchine et al. 2007; van den Bosch et al. 2007).

Interpretations of the mass-metallicity relation generally focus around decreasing star-formation efficiency at low masses, which can suitably explain the trends observed in galaxies (e.g. Tremonti et al. 2004; Savaglio et al. 2005; Gallazzi et al. 2006) and is reproduced in hydrodynamic simulations including feedback mechanisms (e.g. Brooks et al. 2007). In this interpretation of the mass-metallicity relation we expect to see low-mass galaxies trend towards lower  $\alpha$ -element abundances, as the relationship of  $\alpha$ -element abundance to supernovae timescales, namely SNII versus SNIa contributions, provides leverage in separating between rapid, high-efficiency star formation and on-going, low-efficiency star formation (e.g. Terlevich & Forbes 2002; Thomas et al. 2005).

Examining the observed relation of  $[\alpha/Fe]$  with mass in Fig. 5, we find considerable scatter, particularly in galaxies with emission. The majority of this scatter results from increasingly large index errors at low S/N (see Appendix A), but there is also a systematic effect related to our fitting of low-mass, and hence low-metallicity, data. The TMB03 model grids “pinch” together at low  $[Z/H]$ , making the discrimination of  $[\alpha/Fe]$  increasingly difficult (Mendel et al. 2007). So, while we appear to observe significant scatter in the  $[\alpha/Fe]$  measurements of low-mass galaxies, which would generally indicate significant variation in star-formation histories, we are unable to draw any strong conclusions from these data. If we restrict ourselves to galaxies with  $\log M_* \gtrsim 8.5 M_\odot$ , then our data exhibit a weak positive correlation of  $\alpha$ -element enhancement with mass at the  $\sim 95$  percent level, consistent with the interpretation of the mass-metallicity relation as indicative of star-formation efficiency, discussed above.

In our age estimates we see a clear offset between emission-line and passive galaxies, unlike either metallicity or  $\alpha$ -element abundance. The mean stellar age of emission-line galaxies is  $\sim 3.6$  Gyrs, relative to  $\sim 9.1$  Gyrs for passive galaxies. We must, of course, interpret these age measurements with caution as they are strictly luminosity-weighted measurements within our fibre apertures. Emission-line galaxies show a trend of younger central ages towards increasing mass, significant at the  $\sim 2\sigma$  level, which we believe to be largely driven by aperture effects and the centrally concentrated nature of star formation. Analyses of central stellar populations in conjunction with global photometric measurements allow one to constrain the relative fraction of mass contained in central starbursts, which has been found to be of order 10 percent for a range of galaxy masses (e.g. P+08). If we consider the fact that the fraction of galaxy light sampled by AAOmega’s  $2''$  aperture varies by more

<sup>2</sup> Assuming an average metallicity gradient of  $-0.25$  dex per dex, e.g. Sánchez-Blázquez et al. (2007)



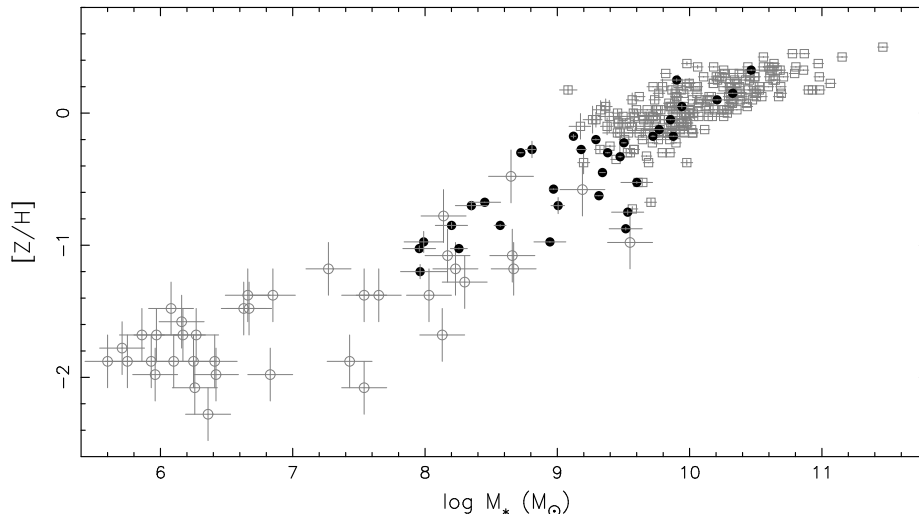


**Figure 6.** Mass–metallicity relation for galaxies spanning a broad range of environments. Filled circles, open circles and open squares represent data from the NGC 5044 group, Local Group and Shapley supercluster respectively. Errors for the Local Group data are taken as the average error quoted in Woo et al. (2008) of 0.17 and 0.2 dex for stellar mass and metallicity. Errors on NGC 5044 group and Shapley supercluster metallicities have been estimated using the Monte Carlo technique described in Section 4.

than an order of magnitude from the brightest to faintest sources in our sample, then the stellar population measurements for our most massive galaxies are almost completely dominated by any central star formation, while in smaller galaxies we sample a growing fraction of the underlying, old stellar populations.

The passive sample of galaxies seems to separate into two sub-samples: one with relatively uniform, old ages ( $\gtrsim 9$  Gyrs), and a second population with relatively young central ages. This younger sub-sample almost certainly represents galaxies which have more recently undergone bursts of star formation and are now fading to older apparent ages. One possible cause for this population could be recent, gas-rich mergers which would serve to drive down central age measurements (e.g. Kauffmann 1996). In this scenario we would expect to see these star-formation bursts accompanied by a decrease in  $\alpha$ -element abundance as new generations of stars form from increasingly metal-enriched gas, however the  $\alpha$ -element abundances for these galaxies are consistent with the bulk of the passive galaxy population.

To summarise, the ages, metallicities and  $\alpha$ -element abundances of galaxies in the NGC 5044 group are consistent with properties found in larger galaxy samples. The tight mass–metallicity relation and its interpretation as a sequence of star-formation efficiency is consistent with our measurements of  $\alpha$ -element abundance, although the trend of elemental abundance with mass appears relatively weak in these data.

## 5.2 The age–mass–metallicity relation

The comparison of galaxy ages, metallicities and element abundances described in the previous section demonstrates the close relationship between metallicity and stellar mass, but it should also be considered that more complex relationships between multiple stellar population parameters and mass may exist. For example, in a study of local early-type galaxies Trager et al. (2000) found that their ellipti-

cal galaxies were described by two separate two-dimensional relations in four-dimensional space: a plane described by the linear combination of  $\log t$ ,  $\log \sigma$  and  $[Z/H]$ , and a relationship between  $[\alpha/Fe]$  and  $\log \sigma$  such that more massive galaxies have higher values of  $\alpha$ -element enhancement. Smith et al. (2008b) found a similar relation between age, mass and metallicity for dwarf galaxies in the Coma cluster, noting in particular an increase in scatter at low masses.

Motivated by recent comparisons suggesting a tight relationship between the properties of galaxies at a fixed *stellar* mass (e.g. van den Bosch et al. 2008), we fit the plane described by our data for age, mass and metallicity such that

$$\log M_* = \alpha [Z/H] + \beta \log t + \gamma, \quad (1)$$

using a least-squares fitting method and minimising residuals orthogonal to the plane. The best-fitting parameters for these data result in a plane such that  $\alpha = 1.83 \pm 0.46$ ,  $\beta = 1.41 \pm 0.79$  and  $\gamma = 9.00 \pm 0.61$ . In Fig. 7 we show projections of this best-fit plane in stellar mass,  $M_*$ , metallicity,  $[Z/H]$ , and age. There is a clear separation between passive and emission-line galaxies about the fitted plane, which is driven primarily by the difference in mean age of the two populations and evident in Fig. 7c. The separation between these two populations is inconsistent with being an effect of the age–metallicity degeneracy in our fits, which primarily moves galaxies along the trends in Fig. 7. If we consider fits to the emission- and non-emission-line galaxies separately, both populations show a similar dependence on stellar mass; the offset between these two populations is dominated by a varying age–metallicity relation. Low-mass galaxies in our sample exhibit an increase in scatter about the fitted plane relative to their high-mass counterparts, in agreement with the observations of Smith et al. (2008b).

The projections shown in Fig. 7 are helpful to examine the distribution of galaxy parameters relative to one another, but are somewhat difficult to interpret in physical terms. In Fig. 8 we show a more standard projection of the

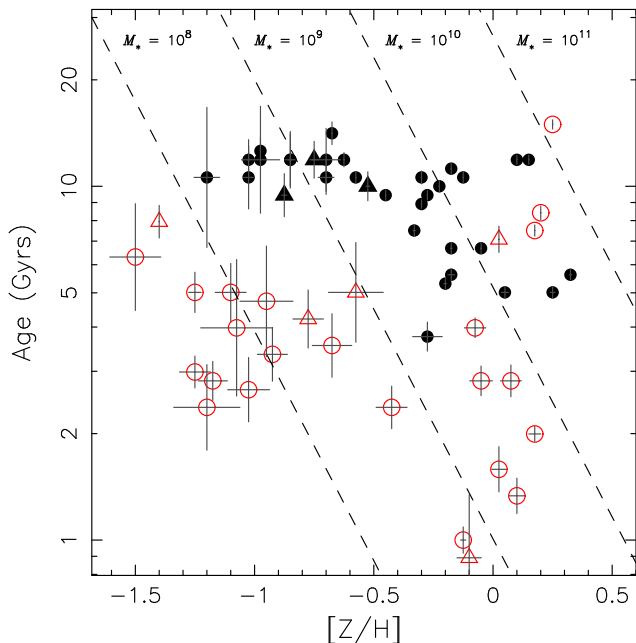


**Figure 8.** Age–metallicity relation for NGC 5044 group galaxies. Symbols are the same as in Fig. 5. Lines of constant stellar mass are shown for  $\log M_* = 8, 9, 10, 11 M_\odot$ . Error bars are the 1-sigma errors determined from Monte Carlo simulations (see §4).

plane in terms of age and metallicity, where *dashed* lines represent the age–metallicity relation at fixed stellar mass as derived from the best-fit plane discussed above.

If we naively interpret the distribution of galaxy ages and metallicities shown in Fig. 8, then there is little evidence for a relationship between central galaxy age and metallicity; galaxies formed at a similar time in the early universe exhibit a spread in metallicity of two or more dex. However, our fits in the age–mass–metallicity plane suggest that this is a flawed conclusion. While it is true to say that there is no clear age–metallicity trend when considering our total sample of galaxies, subsamples of data in narrow mass bins (one or two orders of magnitude) suggest that galaxies with older central ages are more metal poor than centrally young galaxies, supporting evolution of the mass–metallicity relation over time (e.g. Koblunick et al. 2003; Brooks et al. 2007; Lamareille et al. 2007; Maiolino et al. 2008).

### 5.3 Predicted vs. observed colours

While up to this point we have used the BC03 models to derive M/L, and hence mass, for our galaxies, it is important to establish the extent to which these SSP models accurately describe the properties of our sample galaxies. To undertake this comparison we have supplemented the *B*– and *K*–band photometry used in Paper I with *B* – *V* and *g* – *i* colours for a subsample of NGC 5044 group dwarf galaxies presented by Cellone (1999) and Cellone & Buzzoni (2001; 2005; S. Cellone, private communication). Predicted colours are calculated using the BC03 models and measured ages and metallicities. Comparisons of these predictions to our observed colours are shown in Fig. 9.

Galaxies lacking in emission show relatively good agreement with the predicted BC03 colour for their age and

metallicity. This serves as an excellent confirmation in the reliability of M/L estimates for these galaxies which, to some extent, can be seen from the tightness of the mass–metallicity relation in Fig. 5. The scatter in colours of emission line galaxies is considerable, and the causes of this are likely to be two-fold: firstly, we are sampling fundamentally different regions with our spectroscopy and photometry. Whereas this has a negligible effect for passive galaxies, the centrally concentrated star-formation in our emission galaxies means that the colours we predict should be, and indeed are, generally bluer than the observed “global” photometry. In addition, stellar population parameters derived for our emission-line galaxies are the most uncertain, which leads to a greater uncertainty in both our measurements of ages and metallicities and hence a corresponding uncertainty in their predicted colours. Overall, however, the above comparisons suggest that our galaxy data are reasonably well described by the BC03 models.

## 6 GLOBAL PROPERTIES AND GALAXY DISTRIBUTION

We have so far examined general trends in the galaxy population of the NGC 5044 group in their own right. We now turn to a more general discussion of the distribution of galaxy properties within the group.

### 6.1 Stellar population trends with radius

By combining semi-analytic models for star formation and galaxy evolution with recent, large-scale *N*-body simulations such as the Millennium Simulation (Springel et al. 2005), recent theoretical work has made great strides in predicting the distribution of galaxy properties in massive structures like groups and clusters. As an example, de Lucia et al. (2006) found that the luminosity-weighted age, metallicity and stellar mass fall with increasing distance from the cluster centre in their models, out to the virial radius. Given the hierarchical formation scenario favoured in current  $\Lambda$ CDM models these results are not surprising; those galaxies in the highest density regions form first, and subsequent generations of galaxies accreted by the cluster are distributed with radius according to the redshift at which they become cluster members (e.g. Gao et al. 2004). It should be noted, however, that there is considerable scope for the interpretation of projected cluster-centric distance as an indicator of accretion time to be confused by three-body interactions which can eject *bona fide* members to beyond the virial radius (see e.g. Ludlow et al. 2008).

In light of these predictions, we are motivated to examine the radial distribution of stellar populations in the NGC 5044 group. Galaxies residing in groups and clusters for more than a dynamical time should undergo some degree of mass segregation due to the increasing efficiency of dynamical friction with total galaxy mass. In apparently relaxed groups and clusters, such as NGC 5044, we expect any such segregation to be readily apparent. In Paper I we examined the distribution of dwarf and giant galaxies in the NGC 5044 group using *B*-band magnitudes as a simple discriminator between low- and high-mass systems but found no significant evidence for differing radial distributions of these two

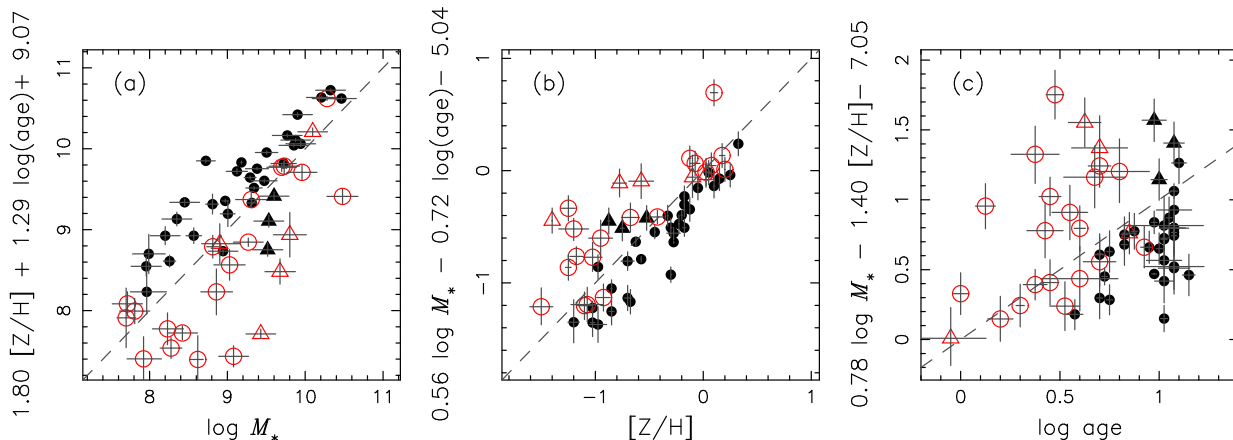


**Figure 7.** Projections of the fitted plane to age, mass and metallicity. Symbols are the same as Fig. 5. *Dashed* lines represent equality and are shown for reference.

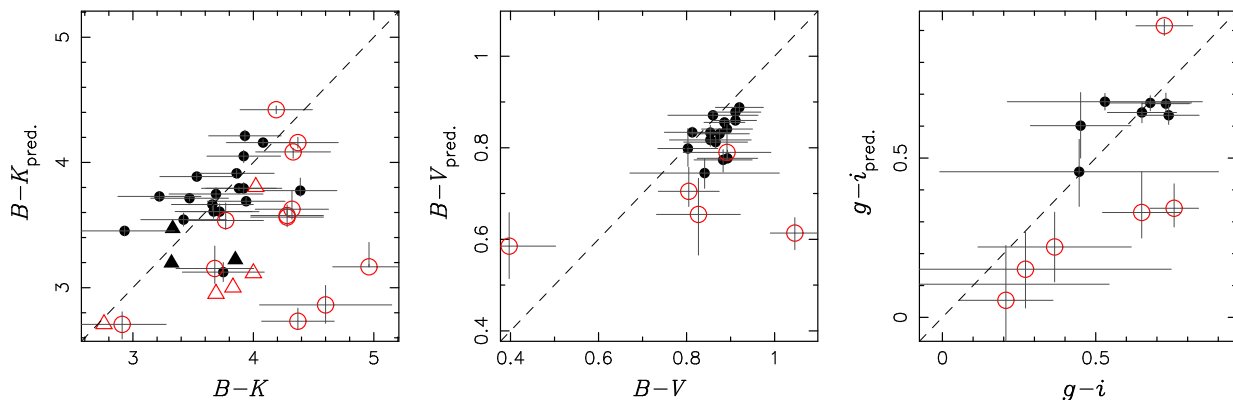


**Figure 9.** BC03 predicted colours vs. observed global  $B-K$ ,  $B-V$  and  $g-i$ . Filled and open symbols represent passive and emission-line galaxies respectively. Errors on predicted colours are calculated using the errors estimates on our central ages and metallicities. *Dashed* lines represent equality between the predicted and observed colours.

sub-populations. Here, we are able to refine this analysis using the stellar masses derived from the BC03 models.

In the upper panels of Fig. 10 we show the distribution of stellar mass, age,  $\alpha$ -element abundance and metallicity in fixed radial bins. In the lower panels we show the radial distribution of galaxies in bins of stellar mass, age,  $\alpha$ -element abundance and metallicity. This figure includes only those galaxies within 500 kpc of the group centre (roughly two-thirds the group’s virial radius) as this is approximately the region observed uniformly with our new AAOmega observations, and thus less prone to spurious, selection-induced trends.

Focusing first on the distribution of properties in fixed radial bins, we find no significant differences in the mean values for age or  $\alpha$ -element abundance (shown by vertical *dashed* lines in the top panels of Fig. 10). Data show some evidence for a deviation in mean galaxy stellar mass and metallicity, and a Kolmogorv-Smirnov (KS) test confirms that metallicities in the inner 150 kpc of the group are inconsistent with being drawn from the same distribution as either of the outer two radial bins at the 2.5 sigma level. Despite the apparent offset in mean stellar mass, a KS test does not find galaxies in the inner group region to have a significantly different mass distribution relative to other radial bins.

Turning to the radial distribution of galaxy properties (Fig. 10, lower panels), a KS test finds that both low-mass and low-metallicity galaxies ( $\log M_* < 8.8$  and  $[Z/H] < -0.7$  dex) exhibit radial distributions that are different to their higher mass and metallicity counterparts. Qualitatively, these differences are evident in Fig. 10 by the clear lack of galaxies from the lowest mass and metallicity bins in the inner 100 kpc of the group centre. The fact that we see this segregation in both mass and metallicity is expected from the tight correlation between these two quantities in our data; the converse holds true for the lack of peculiar distributions in age and  $\alpha$ -element distributions given their lack of a strong correlation with mass.

In order to investigate the relationship between mass, metallicity and radius further, in Fig. 11 we show galaxy metallicities plotted against their group-centric radii, where galaxies have been separated into three separate mass bins. This figure serves as a visual confirmation of the mean offset of galaxy metallicity observed within  $\sim 150$  kpc in Fig. 10, and also shows that this trend is due primarily to a lack of low-mass, and hence low-metallicity, galaxies from the inner 100 kpc of the group. Finally, Fig. 11 suggests that there are no strong radial trends in metallicity at fixed stellar mass.

Previous work by Mathews et al. (2004; hereafter M+04) using the NGC 5044 group catalogue of Ferguson

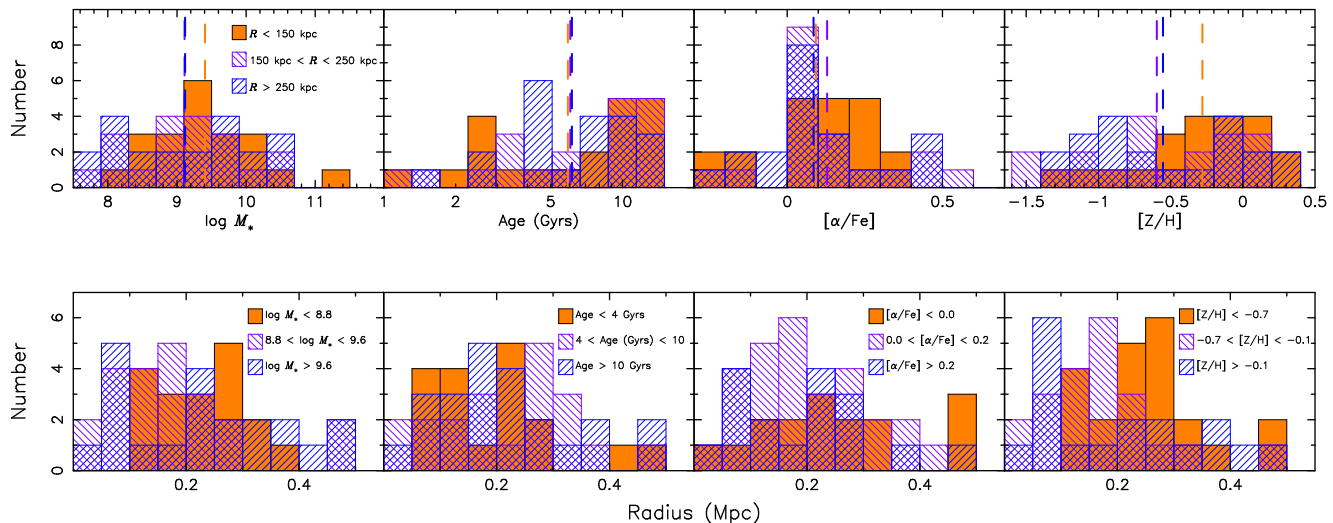


**Figure 10.** The radial dependence of various properties of galaxies in the NGC 5044 group. Top panels show the distribution of stellar mass, age,  $\alpha$ -element abundance and metallicity in three different radial bins of  $R < 150$  kpc,  $150 \text{ kpc} \leq R \leq 250$  kpc and  $R > 250$  kpc (solid orange, green and blue hatched regions respectively). Vertical *dashed* lines show the mean of each bin. Lower panels show the radial distribution of galaxy properties in three separate bins of stellar mass, age,  $\alpha$ -element abundance and metallicity, where bins have been selected to contain roughly equal numbers of galaxies.

& Sandage (1990; hereafter FS90) has noted a similar lack of low-luminosity galaxies in the inner group region. Assuming dwarf galaxies act as tracer particles in the group potential, M+04 compared the cumulative number distribution of dwarf galaxies to the predicted surface mass distribution of a Navarro-Frenk-White (NFW) dark matter profile (Navarro, Frenk & White 1995, 1996, 1997), finding that the NGC 5044 group falls well below the NFW prediction inside  $\sim 300$  kpc. M+04, and later Faltenbacher & Mathews (2005; hereafter FM05), offer two explanations for this apparent central deficit of dwarf galaxies. M+04 argue that a lack of dwarf galaxies could be tied to a low survival rate of low-mass galaxies entering the NGC 5044 group halo at high redshift ( $2 - 3 \leq z \leq 6$ ), or due to suppression of star formation in low-mass galaxies as a result of AGN or outflow activity from the central galaxy. The follow-up work by FM05 showed, using a simple dynamical model, that tidal disruption and dynamical friction could also be responsible for the apparent lack of dwarfs at small radii. In their model, low-mass galaxies approaching the central group potential could be strongly disrupted or destroyed.

Our sample has allowed us to refine the NGC 5044 group membership used by M+04, and we find that limiting the FS90 group samples to only the spectroscopically defined members in Paper I does not significantly alter the conclusions of M+04<sup>3</sup>; there still appears to be a deficit of dwarf galaxies at low projected radii ( $\lesssim 300$  kpc). M+04 suggest that, as a result of low dwarf galaxy survival rates at high redshifts, there should be a relative lack of old, low-mass galaxies in the group. The data presented in Fig. 10 do not suggest any such trend in galaxy ages, with low-mass galaxies appearing similar in mean age to their high-mass counterparts (see also Figs. 5 and 8). In addition, the M+04 scenario would suggest that, relative to massive galaxies, low-mass

dwarf galaxies should be kinematically “younger” in their velocity distribution in the group; in Paper I we find no such evidence for kinematic segregation between high- and low-luminosity galaxies. A repeat analysis of sub-population kinematics using the stellar masses derived in this work gives a similar result, further suggesting that the scenario posed by M+04 does not describe these data in full.

Perhaps the most plausible explanation is that put forward by FM05, where the apparent central deficit of dwarf galaxies is a result of both dynamical friction and tidal disruption. In their work, FM05 find that the evolution of galaxies with stellar to total mass ratios of  $\sim 20$  best describe the population of disrupted galaxies in the NGC 5044 group. Using the relationship between stellar mass and total baryonic mass determined from fits to star-forming galaxies in the SDSS (Baldry, Glazebrook & Driver 2008), we can use the cosmic baryon fraction,  $f_b = 0.171$  as determined from the *WMAP* 5yr results (Komatsu et al. 2008) to estimate the total halo mass for galaxies of a given stellar mass. For the stellar-to-total mass ratio predicted by FM05 of 20, the above relation gives a corresponding stellar mass of  $\log M_* \approx 8.6$ . This is in agreement with the lower limit of stellar mass that we observe in the central 100 kpc of the group centre, providing support for the tidal disruption scenario of FM05.

Confirmation of this would need to come from additional deep imaging to observe the low surface-brightness intragroup light which, given the possibly large number of disrupted or destroyed dwarf galaxies, could be as much as  $\sim 35$  percent of the group’s total luminosity (FM05).

## 6.2 Galaxies and the hot intragroup medium

The metal content of the intracluster/intragroup medium (ICM/IGM) is directly related to the star formation histories of the galaxies via outflows and supernovae driven winds, and therefore provides a useful diagnostic of both

<sup>3</sup> Where the NFW profile is scaled to match the cumulative galaxy distribution at  $\sim 350$  kpc as in M+04

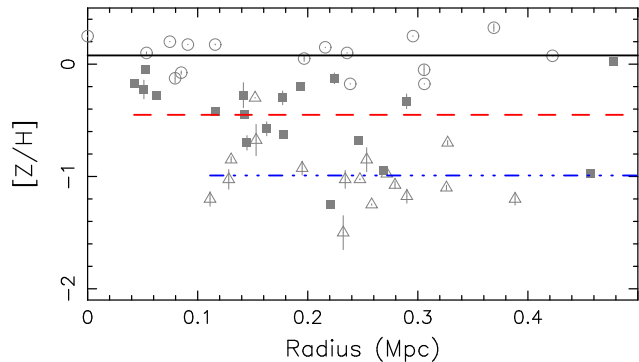


**Figure 11.** Galaxy metallicity against projected group-centric radius. Galaxies are divided into three mass bins with approximately equal numbers such that circles, squares and triangles represent galaxies with  $\log M_* > 9.6$ ,  $8.8 \leq \log M_* < 9.6$  and  $\log M_* \leq 8.8$ . *Solid, dashed and dot-dashed* lines represent the mean metallicity for each mass bin.

group and galaxy evolution. Despite the presence of ongoing evolution in the stellar populations of group and cluster galaxies, observations of high redshift X-ray samples suggest that the bulk of ICM metals were already in place at  $z \sim 1$  (e.g. Tozzi et al. 2003; Balestra et al. 2007) and therefore necessitate that *most* star formation activity and subsequent ICM enrichment takes place at early times.

Rasmussen & Ponman (2007; hereafter RP07) have used *Chandra* archival data to analyse the X-ray abundance properties of 15 nearby groups, including NGC 5044. From their data RP07 extract radial profiles of iron and silicon abundance in the hot IGM out to  $\sim 200$  kpc in NGC 5044, facilitating a comparison between our galaxy stellar population measurements and the chemical properties of the intragroup gas. In Fig. 12 we plot the X-ray derived radial iron and silicon abundances along with the stellar mass-density profiles.

In their abundance analysis of hot gas in the NGC 5044 group, RP07 show that the central silicon to iron ratio is roughly solar (i.e.  $[\text{Si}/\text{Fe}] \sim 0.0$ ), suggesting SNIa are playing an important role in enriching gas in the central group regions. While we lack significant overlap between the X-ray profiles and our binned group profile, the slopes in both iron and silicon abundance in the intragroup gas are consistent with that of the stellar mass density between 50 and  $\sim 100$  kpc. In clusters, the central “excess” of iron in the central regions relative the rest of the ICM is normally attributed to enriched outflows from the central galaxy (e.g. Böhringer et al. 2004). In the case of NGC 5044 this remains a plausible explanation for the high central iron abundance, particularly given recent evidence for large outflows associated with NGC 5044’s central AGN (Temi, Brighenti & Mathews 2007; Gastaldello et al. 2007). We note, however, that our data are also consistent with satellite galaxies having contributed significantly towards building up the central iron peak in the group, particularly given the extended nature of the central excess,  $\sim 50$  kpc, relative to the optical extent of NGC 5044 ( $\sim 20$  kpc; FS90; Paturol et al. 2000; shown with black *dashed* line in Fig. 12) and the the good correspondence between the radial profile of iron abundance and stellar mass-density out to beyond  $\sim 100$  kpc.

In the outer regions,  $R > 100$  kpc, there is evidence for a rising silicon abundance, in contrast to the iron abun-

dance which continues to fall. While the significance of this upturn is only marginal due to its dependence on the outermost measurement in the X-ray data, we have no reason to believe this is a spurious measurement. The observed rise in  $[\text{Si}/\text{Fe}]$  is in agreement with X-ray observations for numerous groups and clusters (e.g. Finoguenov et al. 2000; RP07) and suggests an increased contribution of SNIa relative to SNIa at large projected radii.

To explore the relation between galaxies and the intragroup medium further, in Fig. 13 we show the same binned X-ray abundance profiles as in Fig. 12, only this time overlaid on the radial galaxy trends for metallicity and  $[\alpha/\text{Fe}]$  shown in Fig. 11. This figure clearly shows that both the IGM iron abundance and the  $[\text{Si}/\text{Fe}]$  ratio are well below the average values measured in galaxies at similar radii, despite both iron and silicon declining with radius at a similar rate to the stellar mass-density. On the other hand, low-mass galaxies generally exhibit stellar metallicities which fall below the measured IGM iron abundance at a given radius. Given the shallow potential wells of low-mass galaxies, metal-enhanced starburst or supernovae driven winds provide a plausible explanation for the observed offset (see also Section 5.1). Low-mass galaxies notwithstanding, the observed low chemical abundance of the IGM is consistent with the findings of Buote, Brighenti & Mathews (2004), who also note the low abundance of iron in the IGM relative to the group luminosity (compared to clusters), as well as other work suggesting a high fraction of “primordial” gas in the IGM (e.g. Gibson & Matteucci 1997; Moretti, Portinari & Chiosi 2003).

In terms of silicon abundance, we find a surprising correlation between the rise in  $[\text{Si}/\text{Fe}]$  at  $\sim 100$  kpc and the presence of low-mass, dwarf galaxies at similar radii. If there is a connection between these two observations, it would imply a very high contribution of SNIa relative to SNIa in dwarf galaxies, as well as a significant contribution from these low-mass systems to the total gas mass of the group. Previous studies, however, have shown that, while dwarf galaxies certainly contribute to the reservoir of intragroup gas, it is most likely not significant, constituting *at most* 15% of the total gas mass in clusters (Gibson & Matteucci 1997). This suggests that the connection between these observations is likely only coincidental, particularly given the relatively low IGM iron abundance outside the group core, 10% solar, and the likely sub-solar outflows from dwarf galaxies.

## 7 EMISSION LINE PROPERTIES

Using the sub-sample of our NGC 5044 group with measurable emission lines, we now discuss the emission-line characteristics of our group galaxies, including star-formation rates and nebular metallicities.

First, in order to separate galaxies undergoing star formation activity from those with other strong ionising sources, i.e. AGN, we use a standard emission line diagnostic comparing the  $[\text{OIII}]_{\lambda 5007}/\text{H}\beta$  and  $[\text{NII}]_{\lambda 6584}/\text{H}\alpha$  flux ratios (Baldwin, Phillips & Terlevich 1981), shown in Fig. 14. We use two predictions to characterise the emission line flux ratios of our galaxies. The first is the theoretical maximum starburst limit calculated by Kewley et al. (2001; *dashed* line in Fig. 14), while the second is the semi-empirical limit of

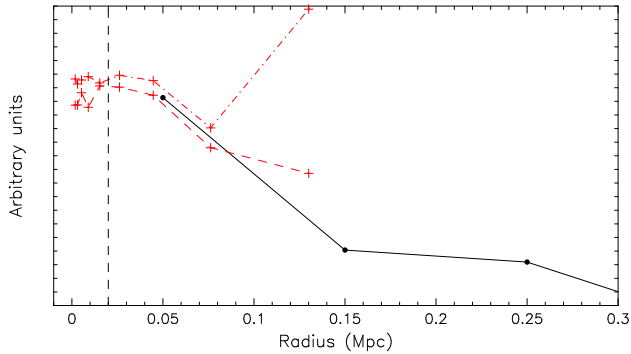


**Figure 12.** Comparison of stellar mass density (*solid black line*) and X-ray derived iron and silicon abundances (*red dashed and dot-dashed lines* respectively) as a function of radius. Data have had a fixed offset applied to be shown on the same figure. X-ray data have been binned for clarity. The vertical *dashed line* represents the radial extent of NGC 5044’s light profile of  $\sim 20$  kpc.

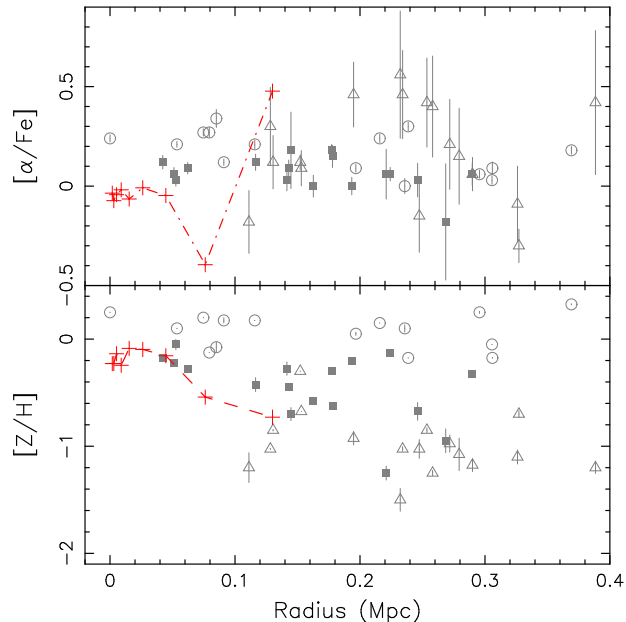


**Figure 13.** Comparison of X-ray derived silicon and iron abundance profiles (*dashed lines* in each panel) with the distribution of galaxy  $\alpha$ -element abundances and metallicities. Galaxy symbols are the same as in Fig. 11. X-ray data have been binned for clarity.

pure star formation defined by Kauffmann et al. (2003) using a large sample of SDSS emission line galaxies (*solid line* in Fig. 14). These lines separate our sample into galaxies which are purely star-forming, strongly AGN or ionised by a composite source (some contribution from both AGN and star-formation), shown with circles, triangles and squares in Fig. 14.

NGC 5044 is known to host AGN activity (Ricketts, Pastoriza & Bonatto 2004, Brough et al. 2007) and is identified as such in Fig. 14, but we also identify two other group galaxies as hosts of potential AGN or other strong ionising sources: NGC 5037 (FS 068) and FS 082. The classification of these galaxies as AGN sources is supported by the available *Chandra* data, in which all three galaxies are detected.

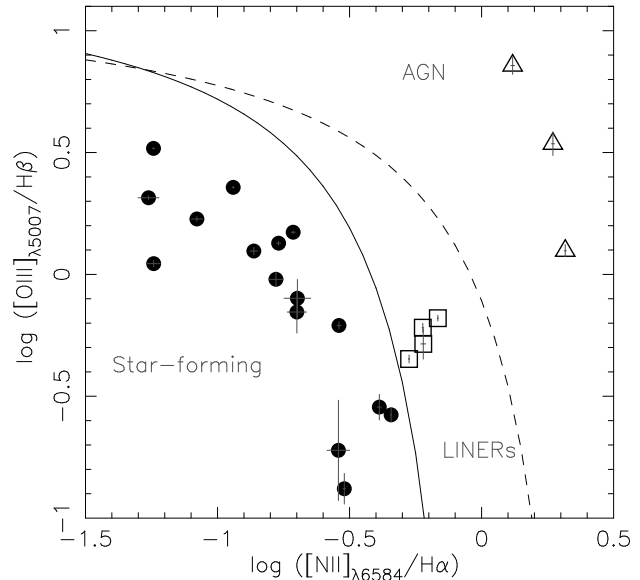


**Figure 14.** Line diagnostic for emission galaxies in our NGC 5044 group sample. The *solid* and *dashed* lines represent the semi-empirical pure star formation line from Kauffmann et al. (2003) and the theoretical maximum starburst line from Kewley et al. (2001) respectively. Symbols represent galaxies which are likely purely star-forming, AGN or composite AGN and star-forming (circles, open triangles and open squares respectively).

## 7.1 Star formation rate

In large samples, comparisons of galaxy properties with local environment show strong evidence for a decreasing fraction of star-forming galaxies in regions of higher projected galaxy surface density (Lewis et al. 2002; Gómez et al. 2003; Poggianti et al. 2006). Even at relatively low gas densities, such as those found in groups, recent work has shown that ram-pressure stripping can influence star-formation via depletion of a galaxy’s hot-gas reservoir (Sivakoff et al. 2004; Machacek et al. 2005; Rasmussen et al. 2006; Kawata & Mulchaey 2008). However in higher-density environments, such as the Coma cluster, Poggianti et al. (2004) have found evidence for young post-starburst galaxies preferentially located near the edges of X-ray substructures. These observations suggest that galaxy–ICM interactions may play a key role in the truncation of star formation, but may equally contribute to initiating bursts of star formation in galaxies as they encounter dense environments.

In our own data, varying fibre throughput and sensitivity make proper flux calibration of our data difficult and therefore limit our ability to derive absolute measurements of the star formation rate, SFR, using  $H\alpha$  line fluxes. Instead, we use the relation derived by Guzmán et al. (1997) to estimate star formation rates using  $B$ -band luminosity and [OII] equivalent widths, where

$$\text{SFR}(M_{\odot}\text{yr}^{-1}) \approx 2.47 \times 10^{-12} L_B(L_{\odot}) \text{EW}_{[\text{OII}]}. \quad (2)$$

We use the  $B$ -band luminosities for galaxies as published in Paper I, which are taken from FS90 and Paturel et al. (2005).

The use of [OII] instead of  $H\alpha$  introduces an additional error into the estimation of the star formation rate of order 0.2 to 0.3 dex (Kewley et al. 2004). The relation fit by Guzmán et al. (1997) to convert between [OII] flux and

[OII] equivalent width carries with it increased uncertainty of  $\sim 0.1$  dex in the derived SFR. Given these two relatively significant error contributions, in addition to the relatively large errors in the FS90 and Paturel et al. photometry (0.5 and 0.3 dex respectively, see Paper I), we consider our star formation rates to only be proportional to the star formation activity in any given galaxy, but by no means a clear indicator of the absolute star formation rate.

In Fig. 15 we show the specific star formation rate for galaxies as estimated using Eqn. 2 in relation to their projected radius from the group centre. The star formation rates shown in Fig. 15 have been normalised by the galaxy stellar mass and are shown in units of  $\text{yr}^{-1}$  per  $10^9 M_{\odot}$ . We see no clear correlation of SFR with radius, and results are similar if we consider projected galaxy density. Motivated by the possible dependence of SFR on galaxy–ICM/IGM interaction, we have also examined the star formation rate relative to a simple expression proportional to the IGM ram pressure,  $P_{\text{ram}} = \rho(r)|\bar{v}_{\text{group}} - \nu|^2$ , where  $\rho(r)$  is the IGM density and  $|\bar{v}_{\text{group}} - \nu|$  is the galaxy velocity  $\nu$  relative to systemic group velocity  $\bar{v}_{\text{group}}$ . Assuming that  $\rho(r) \propto r^{-2}$ , we then arrive at a comparison of SFR against  $|\bar{v}_{\text{group}} - \nu|^2/r^2$ , which shows a similar lack of correlation as the radial and galaxy density comparisons described above. We note that projection effects are likely having a strong effect on any of our radial SFR comparisons as we cannot properly relate our galaxy positions and recession velocities to their true position and relative motion within the group. Nevertheless, while these data do not allow us rule out the role of interactions with intragroup gas as influencing the observed star formation in these galaxies, they seem to hint that these effects are relatively limited in this case.

An alternative possibility for triggering or enhancing star formation is through galaxy–galaxy interactions. Hydrodynamic simulations modelling gas have shown that tidal interactions can enhance or induce central star formation by driving gas from the disk to the central regions (e.g. Barnes & Hernquist 1992; Di Matteo et al. 2007), which supports observations of enhanced star formation in close pairs of galaxies (e.g. Lin et al. 2007; Ellison et al. 2008). An examination of DSS images for the 22 galaxies with [OII] emission shows that only 2 galaxies, FS90 134 and FS90 137, exhibit clear evidence for ongoing interaction. Several other galaxies show some evidence of disturbed morphology (i.e. boxy bulges and disturbed disks), however it appears that the majority of recent star formation activity we see in the NGC 5044 group is not driven by currently ongoing galaxy–galaxy interactions.

## 7.2 Emission-line metallicity

Nebular metallicity and underlying, stellar metallicity are intimately related via star formation. The evolution of stellar metallicity (as measured by absorption features) is strictly dependent on a galaxy’s star formation history, while nebular metallicities continue to vary as previous generations of stars evolve and enrich the interstellar medium. We are therefore able to use the relative offset of emission- and absorption-line metallicities to extract information related to the last significant star formation episode. Here we use a reparameterisation of the Kewley & Dopita (2002; hereafter KD02)  $R_{23}$  method presented by Kobulnicky & Kew-

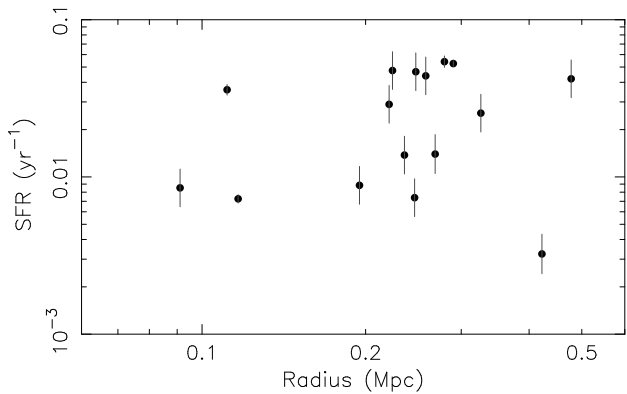


**Figure 15.** Specific star formation rate as it varies with projected distance from the group centre. Errors are indicative of the uncertainty in our  $\text{EW}_{[\text{OII}]}$  and  $B$ -band luminosity measurements, but do not include the systematic contribution from using [OII] over  $\text{H}\alpha$  and equivalent widths as opposed to line fluxes (see §7.1).

ley (2004; hereafter KK04) to derive gas-phase metallicities for a subsample of our emission-line galaxies. We exclude from this analysis galaxies exceeding the maximum starburst limit shown in Fig. 14 as likely hosting AGN (NGC 5044, NGC 5037 and FS 082).

The  $R_{23}$  metallicity calibrator is typically defined using emission line fluxes, however this requires spectra to be properly flux calibrated as line ratios spanning a significant wavelength range will otherwise be incorrect. An alternate approach is to use measurements of equivalent width in place of line fluxes to compute  $\text{EW-}R_{23}$ , which avoids the issues of flux calibration and extinction correction, but introduces the problem of potential variation in the underlying stellar continua (particularly between old and young spectra). In a statistical sense, the variation between  $R_{23}$  and  $\text{EW-}R_{23}$  results in an additional error on the final metallicity determination of  $\sim 0.11$  dex (Kobulnicky & Phillips 2003), however in our relatively small sample where we *know* the underlying stellar populations vary significantly, the uncertainty between  $R_{23}$  and  $\text{EW-}R_{23}$  can have a potentially significant effect on our results. Considering both the wide range of spectra types and uncertain flux calibration of our data, we estimate nebular metallicities using both  $R_{23}$  and  $\text{EW-}R_{23}$ . Since the effects of varying stellar continua and flux calibration affect emission-line metallicity measurements differently, by using both of these measurements we can assess the reliability of our conclusions.

Comparison of  $\text{EW-}R_{23}$  and  $R_{23}$  shows that the scatter between the two measures is  $\sim 0.08$  dex, or  $\sim 0.11$  dex in terms of the final determination of  $12 + \log(\text{O}/\text{H})$  (Kobulnicky & Phillips 2003), which is generally less than the intrinsic error in the calibration of  $R_{23}$  to nebular oxygen abundance. In our own data, the scatter between  $\text{EW-}R_{23}$  and  $R_{23}$  is  $\sim 0.16$  dex, but this scatter is primarily driven by two galaxies with significant offsets between  $\text{EW-}R_{23}$  and  $R_{23}$ . Excluding these galaxies the scatter on our data falls to  $\sim 0.07$  dex. We therefore exclude these deviant galaxies from the remainder of our emission line analyses and consider measurements on the remaining galaxies to be reliable.

Comparison of stellar and nebular metallicities is carried out by converting nebular oxygen abundances to the implied metal mass fraction using the relation  $Z \simeq 29 \times$

$10^{[12+(O/H)]-12}$ , assuming the standard solar abundance distribution and solar oxygen abundance of  $12 + (O/H) = 8.72$  (Allende Prieto, Lambert & Asplund 2001; Kobulnicky & Kewley 2004). In Fig. 16 we show the comparison between the converted nebular metallicities and stellar metallicity. We find that, in general, derived nebular metallicities are super-solar, and in some cases nearly 1 dex higher than their stellar counterparts. The relatively shallow relation between stellar and nebular metallicities is somewhat puzzling, as it implies a significantly weaker mass-metallicity relation among star-forming galaxies than is generally observed (e.g. Tremonti et al. 2004).

Given this somewhat curious result we are motivated to examine the relative difference between nebular and stellar metallicity as a function of other galaxy properties. In Fig. 17, the relative offset between nebular and stellar metallicity is plotted against galaxy stellar mass, age and  $\alpha$ -element abundance. The relationship between metallicity offset and stellar mass in Fig. 17 is driven primarily by the mass-metallicity relation and shows that the most massive galaxies have the lowest measured nebular–stellar metallicity offsets as a result of the relatively uniform, high nebular metallicities measured.

In terms of age, those galaxies with the lowest metallicity offsets also have the youngest luminosity-weighted ages, which is consistent with the observed stellar population forming recently from gas present in these galaxies. Interestingly, while the trend of metallicity offset with age is consistent with our understanding of galaxy formation, the magnitude of this offset is large, nearly 1.5 dex in the case of the lowest-mass galaxies. This offset is difficult to explain through pure passive evolution of the stellar populations in these galaxies, i.e. through enrichment from SNII and SNIa, which in extreme cases can account for  $\sim 1$  dex of metallicity increase (see, e.g. Sansom & Proctor 1998). An alternate explanation is that *ongoing* star formation has helped to enhance the observed gaseous metallicities through the evolution of metal-enriched stars. In this case the integrated stellar populations should also appear both younger and more metal rich in those galaxies hosting the largest nebular–stellar metallicity offsets, in conflict with the trends in Fig. 17. Finally, these data could be explained in a scenario where the gas reservoirs of low-mass galaxies are being preferentially depleted over high-mass galaxies, which would increase the effect of any subsequent enrichment due to supernovae.

In order to explain these observations in terms of gas removal, we require that the removal process must be more efficient in low-mass galaxies, ruling out AGN activity as a possibility due to its strong scaling with mass. Starburst outflows, primarily driven by SNII, satisfy the above stated mass dependence but would also likely affect the observed  $[\alpha/Fe]$  ratio of stars formed from any remaining gas, in conflict with Fig. 17c. Galaxy–IGM interactions such as ram-pressure stripping (Gunn & Gott 1982) and viscous stripping (Nulsen 1982) satisfy both the inverse mass dependence and non-preferential gas removal (i.e. gas-phase metals from SNII and SNIa must be removed more-or-less equally) stipulated by these observations. Strictly speaking, we cannot rule out any processes from contributing to the observed galaxy processes, however our data are best explained by galaxy–IGM dominating gas removal in the NGC 5044 group.

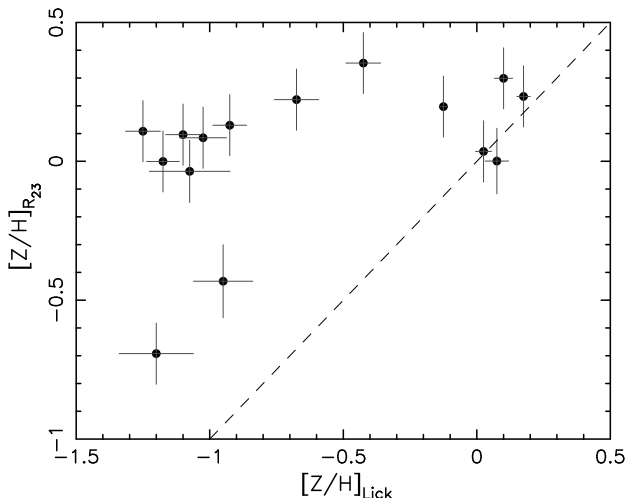


**Figure 16.** Comparison of metallicity derived from the nebular oxygen abundance,  $[Z/H]_{R23}$  and stellar metallicity,  $[Z/H]_{Lick}$ , derived using Lick indices. The *dashed* line represents equality between the nebular and stellar metallicities.

## 8 DISCUSSION AND CONCLUSIONS

In this second of two papers, we have undertaken a spectroscopic investigation of galaxies in the group environment, deriving stellar masses, ages, metallicities and  $\alpha$ -element abundance ratios for 67 of the 111 spectroscopically confirmed NGC 5044 group members described by Mendel et al. (2008). These measurements have allowed us to examine the star formation histories of these group members, both as a population in their own right and in the context of the group environment and their location in it.

The mass–metallicity relation plays a fundamental role in describing galaxy populations, and we see strong evidence of this in the overall tightness of the mass–metallicity relation in our group data over multiple orders of magnitude in stellar mass. In the context of environment, by comparing the mass–metallicity relation of NGC 5044 group galaxies with galaxies in the local group and the Shapley supercluster, we show that galaxies appear to form a continuous mass–metallicity relation across several orders of magnitude in system mass and spanning upwards of six orders of magnitude in galaxy stellar mass. These data argue for a relative independence of the mass–metallicity relation from environment (e.g. Maiolino 2008; van den Bosch et al. 2008).

In terms of galaxy ages and  $\alpha$ -element abundances, we find no evidence for strong trends with galaxy mass. Our  $\alpha$ -element abundance data do not rule out the interpretation of star formation efficiency as the primary driver of the mass–metallicity relation. Particularly at higher stellar masses ( $\log M_* \gtrsim 9 M_\odot$ ) and metallicities, where wide separation of model grids allow for finer abundance measurements, our data show hints of a trend of increasing  $\alpha$ -element ratio with mass, consistent with literature results (e.g. Terlevich & Forbes 2002; Thomas et al. 2005). We have shown that the surface described simultaneously by age, mass and metallicity is vital to analyses of galaxy data spanning a broad range in mass. Most notably, mass dependence is vital to interpretation of the galaxy age–metallicity relation.

In terms of the galaxy radial distribution, we find no apparent radial dependence in either age or  $\alpha$ -element abun-



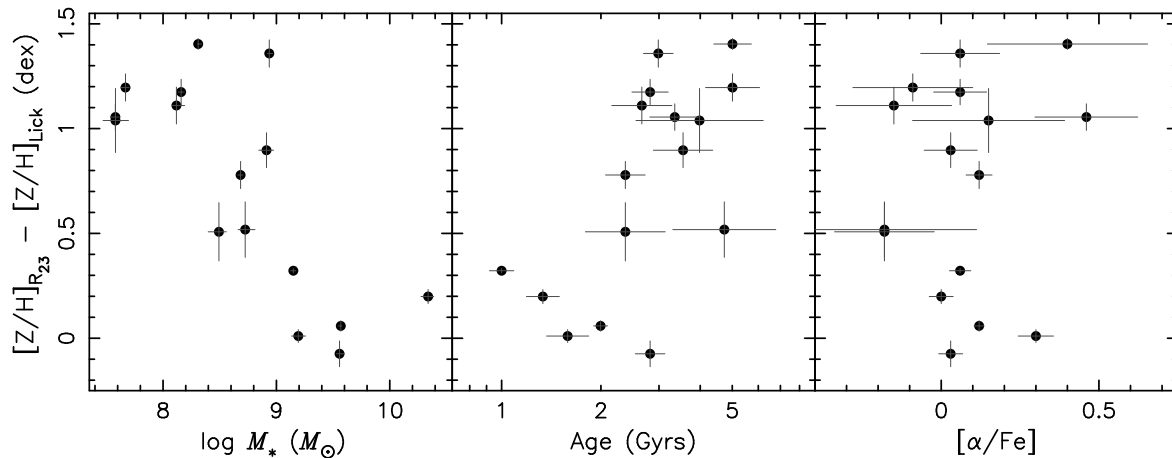


Figure 17. Offset between nebular and stellar metallicity plotted against stellar mass, age and  $\alpha$ -element abundance.

dances. A KS test finds that low-mass and low-metallicity galaxies have radial distributions inconsistent with their high-mass and high-metallicity counterparts, and an examination of this apparent difference shows that we observe *no* galaxies with  $\log M_* \lesssim 8.9 M_\odot$  within  $\sim 100$  kpc projected radius from the group centre. In the context of previous analyses of the NGC 5044 group, M+04 and FM05 have both noted the apparent lack of dwarf galaxies in the group’s central regions using the photometric catalogue of FS90. Our spectroscopic observations confirm that the dwarf galaxy distribution observed by M+04 and FM05 is not due to the inclusion of significant foreground or background contamination in the FS90 catalogue (see Paper I). Of the possible scenarios for explaining this deficit, the most plausible seems to be that dwarf galaxies are being tidally disrupted or destroyed through interactions with the group or central galaxy potential. Our data are consistent with the simulations of FM05 in their prediction of stellar-to-total mass ratios for disrupted galaxies of  $\sim 20$ , corresponding to  $\sim \log M_* \approx 8.6$ . Deep wide-field imaging is required to confirm this conclusion, as the models of FM05 predict stars from the disrupted population of dwarf galaxies to contribute nearly 35 percent of the total group luminosity, consistent with estimates of intracluster light for other groups at a similar mass (e.g. Gonzalez, Zaritsky & Zabludoff 2007).

With regard to similar types of analyses on other groups and clusters, Coma is the only cluster analysed to a similar depth with stellar population measurements. Smith et al. (2008a) have examined radial gradients of Coma cluster dwarf galaxies, finding strong trends towards younger ages and higher metallicities with increasing cluster-centric radii. While these results are at odds with our own, we believe this disagreement to be largely driven by the galaxy selection employed by Smith et al. (2008a). The trends observed by Smith et al. (2008a) are consistent with the interpretation that the south-west “infall” region of Coma has already undergone a passage through the cluster centre. Observations of younger ages and higher metallicities in a “quenched” dwarf population would then be consistent with the idea of induced star formation from galaxy encounters with the dense/hot IGM (e.g. Poggianti et al. 2004). The fact that we do not see such a trend would seem to suggest that we either fail to measure galaxies at sufficient radii to

see effects of induced star formation in our galaxies, or that such dramatic interactions are not occurring within the central regions we probe here. It is worth noting that in Paper I we identified a possible infalling substructure to the north-east of NGC 5044 at  $\sim 1.4$  Mpc projected separation, but our stellar population measurements do not extend that far and so we are unable to comment on possible trends at these large radii.

While we do not see any obvious trends of stellar populations with radius, as Smith et al. do, we do perhaps find a more subtle interpretation of galaxy evolution in the group environment through analysis of emission-line properties. Comparison of emission- and absorption-line metallicities has allowed us to extract information regarding the previous star-formation episodes of galaxies through the relation of nebular and stellar metallicities. What we find is that the relative offset between these two metallicity estimates is too large to be explained by either pure passive evolution of galaxies, which can account for at most  $\sim 1$  dex of offset, or ongoing star formation, which is inconsistent with other observed galaxy properties. The mass-dependence of our emission-absorption metallicity offset instead is consistent with a scenario in which galaxies are being stripped of their gas primarily through galaxy-IGM interactions, and therefore subsequent ISM enrichment is having a larger effect on the observed emission-line metallicity. We require a larger sample of galaxies to confirm such an analysis, however this method provides a novel technique for probing environmental effects on galaxy evolution.

We turn, finally, to the question of NGC 5044’s evolution as a group and what information the galaxy population holds in this regard. The relative lack of radial trends in the stellar population data limit the extent to which the gradual accretion scheme present in semi-analytic models of group formation (e.g. de Lucia et al. 2006; Berrier et al. 2008) can be acting in the NGC 5044 group, at least without considerable mixing of the galaxy distribution with radius (e.g. Ludlow et al. 2008). The large peculiar velocity of NGC 5044 itself relative to the group mean ( $\sim 200 \text{ km s}^{-1}$ ), possible presence of substructure on the outer regions of the group (see Paper I) and recent detection of a “sloshing” type cold front in the group’s X-ray distribution (Gastaldello et al. 2008) suggest that the group is still growing and in the process

of relaxation. However, the group's Gaussian line-of-sight velocity distribution and relatively uniform X-ray profiles argue against any recent, dynamically violent evolution of the group.

The work presented here represents the first targeted effort at constraining the stellar population trends of group galaxies. Further work is clearly needed, particularly on larger samples of homogeneously selected galaxies, to better constrain the processes driving galaxy evolution in groups.

## ACKNOWLEDGEMENTS

The authors would like to thank the anonymous referee for his/her helpful comments and suggestions. We would also like to thank Marc Sarzi for his help in using GANDALF and Sergio Cellone for providing us with his imaging and photometric measurements of dwarf galaxies in the NGC 5044 group.

We acknowledge the analysis facilities provided by IRAF, which is distributed by the National Optical Astronomy Observatories, which is operated by the Association of Universities for Research in Astronomy, Inc., under cooperative agreement with the National Science Foundation. This publication makes use of data products from the Two Micron All Sky Survey, which is a joint project of the University of Massachusetts and the Infrared Processing and Analysis Center/California Institute of Technology, funded by the National Aeronautics and Space Administration and the National Science Foundation. We also thank the Australian Research Council for funding that supported this work.

## REFERENCES

- Abadi M. G., Moore B., Bower R. G., 1999, MNRAS, 308, 947  
 Allende Prieto C. A., Lambert D. L., Asplund M., 2001, ApJ, 556, 63  
 Baldry I. K., Balogh M. L., Bower R. G., Glazebrook K., Nichol R. C., Bamford S. P., Budavari T., 2006, MNRAS, 373, 469  
 Baldry I. K., Glazebrook K., Driver S. P., 2008, MNRAS, 388, 945  
 Baldwin J. A., Phillips M. M., Terlevich R., 1981, PASP, 93, 5  
 Balestra I., Tozzi P., Ettori S., Rosati P., Borgani S., Mainieri V., Norman C., Viola M., 2007, A&A, 462, 429  
 Balogh M. L., Morris S. L., 2000, MNRAS, 318, 703  
 Barnes J. E., Hernquist L., 1992, ARA&A, 30, 705  
 Beasley M. A., Brodie J. P., Strader J., Forbes D. A., Proctor R. N., Barmby P., Huchra J. P., 2004, AJ, 128, 1623  
 Böhringer H., Matsushita K., Churazov E., Finoguenov A., Ikebe Y., 2004, A&A, 416, 21  
 Bell E. F., de Jong R. S., 2001, ApJ, 550, 212  
 Bell E. F., et al., 2004, ApJ, 608, 752  
 Berrier J. C., Stewart K. R., Bullock J. S., Purcell C. W., Barton E. J., Wechsler R. H., 2008, preprint (astro-ph/0804.0426)  
 Blanton M. R., et al., 2003, ApJ, 592, 819  
 Blanton M. R., Eisenstein D., Hogg D. W., Schlegel D. J., Brinkmann J., 2005, ApJ, 629, 143  
 Blanton, M. R., Berlind A. A., 2007, ApJ, 664, 791  
 Brooks A. M., Governato F., Booth C. M., Willman B., Gardner J. P., Wadsley J., Stinson G., Quinn T., 2007, ApJ, 655, 17  
 Brown M. J. I., Dey A., Jannuzi B. T., Brand K., Benson A. J., Brodwin M., Croton D. J., Eisenhardt P. T., 2007, ApJ, 654, 858  
 Brough S., Proctor R., Forbes D. A., Couch W. J., Collins C. A., Burke D. J., Mann R. G., 2007, MNRAS, 378, 1507  
 Bruzual G., Charlot S., 2003, MNRAS, 344, 1000 (BC03)  
 Burstein D., Faber S. M., Gaskell C. M., Krumm N., 1984, ApJ, 287, 586  
 Bundy K., et al., 2006, ApJ, 651, 120  
 Buote D. A., Brighenti F., Mathews W. G., 2004, ApJ, 607, 91  
 Caldwell N., Rose J. A., Sharples R. M., Ellis R. S., Bower R. G., 1993, AJ, 106, 473  
 Caldwell N., Rose J. A., Concannon K. D., 2003, AJ, 125, 2891  
 Cardelli J. A., Clayton G. C., Mathis J. S., 1989, ApJ, 345, 245  
 Carter D., et al., 2002, ApJ, 567, 772  
 Cappellari M., Emsellem E., 2004, PASP, 116, 138  
 Cellone S. A., 1999, A&A, 345, 403  
 Cellone S. A., Buzzoni A., 2001, A&A, 369, 742  
 Cellone S. A., Buzzoni A., 2005, MNRAS, 356, 41  
 Chabrier G., 2003, PASP, 115, 763  
 Conroy C., Gunn J. E., White M., 2008, preprint (astro-ph/0809.4261)  
 Cooper M. C., Tremonti C. A., Newman J. A., Zabludoff A. I., 2008, arXiv:0805.0308  
 De Lucia G., Springel V., White S. D. M., Croton D., Kauffmann G., 2006, MNRAS, 366, 499  
 Di Matteo P., Combes F., Melchior A.-L., Semelin B., 2007, A&A, 468, 61  
 Dressler A., 1980, ApJ, 236, 351  
 Ellison S. L., Patton D. R., Simard L., McConnachie A. W., 2008, AJ, 135, 1877  
 Faber S. M., et al., 2007, ApJ, 665, 265  
 Faltenbacher A., Mathews W. G., 2005, MNRAS, 362, 498 (FM05)  
 Farouki R., Shapiro S. L., 1981, ApJ, 243, 32  
 Ferguson H. C., Sandage A., 1990, AJ, 100, 1 (FS90)  
 Finoguenov A., David L. P., Ponman T. J., 2000, ApJ, 544, 188  
 Gallazzi A., Charlot S., Brinchmann J., White S. D. M., 2006, MNRAS, 370, 1106  
 Gao L., White S. D. M., Jenkins A., Stoehr F., Springel V., 2004, MNRAS, 255, 819  
 Gibson B. K., Matteucci F., 1997, ApJ, 475, 435  
 Gómez P. L., et al., 2003, ApJ, 584, 210  
 Gonzalez A. H., Zaritsky D., Zabludoff A. I., 2007, ApJ, 666, 147  
 Goto T., Yamauchi C., Fujita Y., Okamura S., Sekiguchi M., Smail I., Bernardi M., Gómez P. L., 2003, MNRAS, 346, 601  
 Gastaldello F., Buote D. A., Temi P., Brighenti F., Mathews W. G., Ettori S., 2008, arXiv:0807.3526  
 Gunn J. E., Gott J. R., 1972, ApJ, 176, 1  
 Guzman R., Gallego J., Koo D. C., Phillips A. C., Lowenthal J. D., Faber S. M., Illingworth G. D., Vogt N. P., 1997, ApJ, 489, 559  
 Hester J. A., 2006, ApJ, 647, 910  
 Hogg D. W., et al., 2002, AJ, 124, 646  
 Jarrett T. H., Chester T., Cutri R., Schneider S., Skrutskie M., Huchra J. P., 2000, AJ, 119, 2498  
 Jensen J. B., Tonry J. L., Barris B. J., Thompson R. I., Liu M. C., Rieke M. J., Ajhar E. A., Blakeslee J. P., 2003, ApJ, 583, 712  
 Jimenez R., Bernardi M., Haiman Z., Panter B., Heavens A. F., 2007, ApJ, 669, 947  
 Jones D. H., et al., 2004, MNRAS, 355, 747  
 Jones D. H., Saunders W., Read M., Colless M., 2005, PASA, 22, 277  
 Jørgensen L., Franx M., Kjaergaard P., 1995, MNRAS, 276, 1341  
 Kauffmann G., 1996, MNRAS, 281, 487  
 Kauffmann G., et al., 2003, MNRAS, 346, 1055  
 Kauffmann G., White S. D. M., Heckman T. M., Ménard B., Brinchmann J., Charlot S., Tremonti C., Brinkmann J., 2004, MNRAS, 353, 713  
 Kawata D., Mulchaey J. S., 2008, ApJ, 672, 103

- Kewley L. J., Dopita M. A., Sutherland R. S., Heisler C. A., Trevena J., 2001, *ApJ*, 556, 121
- Kewley L. J., Geller M. J., Jansen R. A., 2004, *AJ*, 127, 2002
- Kewley L. J., Dopita M. A., 2002, *ApJS*, 142, 35
- Kobulnicky H. A., et al., 2003, *ApJ*, 599, 1006
- Kobulnicky H. A., Kewley L. J., 2004, *ApJ*, 617, 240
- Kobulnicky H. A., Phillips A. C., 2003, *ApJ*, 599, 1031
- Komatsu E., et al., 2008, preprint (astro-ph/0803.0547)
- Korn A. J., Maraston C., Thomas D., 2005, *A&A*, 438, 685
- Lamareille F., Contini T., Charlot S., Brinchmann J., 2007, in Combes F., Palous J., ed., *IAU Symposium 235, Galaxy Evolution Across the Hubble Time*, Cambridge University Press, p. 408
- Larson R. B., Tinsley B. M., Caldwell C. N., 1980, *ApJ*, 237, 692
- Lewis I., et al., 2002, *MNRAS*, 334, 673
- Lin L., et al., 2007, *ApJ*, 660, 51
- Ludlow A. D., Navarro J. F., Springel V., Jenkins A., Frenk C. S., Helmi A., 2008 preprint (astro-ph/0801.1127v1)
- Machacek M. E., Nulsen P., Stirbat L., Jones C., Forman W. R., 2005, *ApJ*, 630, 280
- Maiolino R., 2008, *A&A*, 488, 463
- Mathews W. G., Chomiuk L., Brighenti F., Buote D. A., 2004, *ApJ*, 616, 745 (M+04)
- McIntosh D. H., Guo Y., Hertzberg J., Katz N., Mo H. J., van den Bosch F. C., Yang X., 2008, *MNRAS*, 388, 1537
- Mendel J. T., Proctor R. N., Forbes D. A., 2007, *MNRAS*, 379, 1618
- Mendel J. T., Proctor R. N., Forbes D. A., Brough S., 2008, *MNRAS*, 389, 749 (Paper I)
- Mobasher B., et al., 2001, *ApJS*, 137, 279
- Moore B., Katz N., Lake G., Dressler A., Oemler A., 1996, *Nature*, 379, 613
- Mouchine M., Gibson B. K., Renda A., Kawata D., 2008, preprint (astro-ph/0801.2476)
- Moretti A., Portinari L., Chiosi C., 2003, *A&A*, 408, 431
- Navarro, J. F., Frenk C. S., White S. D. M., 1995, *MNRAS*, 275, 56
- , 1996, *ApJ*, 462, 563
- , 1997, *ApJ*, 490, 493
- Negroponte J., White S. D. M., 1983, *MNRAS*, 205, 1009
- Nulsen P. E. J., 1982, *MNRAS*, 198, 1007
- Oemler A., 1974, *ApJ*, 194, 1
- O'mill A. L., Padilla N., Lambas D. G., 2008, *MNRAS*, 389, 1763
- Osterbrock D. E., 1989, *Astrophysics of gaseous nebulae and active galactic nuclei*, University Science Books
- Paturel G., Fang Y., Petit C., Garnier R., Rousseau J., 2000, *A&AS*, 146, 19
- Paturel G., Vauglin I., Petit C., Borsenberger J., Epchtein N., Fouqué P., Mamon G., 2005, *A&A*, 430, 751
- Peletier R. F., 2007, *MNRAS*, 379, 445
- Pierce M. et al., 2006, *MNRAS*, 366, 1253
- Poggianti B. M., Bridges T. J., Komiyama Y., Yagi M., Carter D., Mobasher B., Okamura S., Kashikawa N., 2004, *ApJ*, 601, 197
- Poggianti B. M., et al., 2006, *ApJ*, 642, 188
- Proctor R. N., Forbes D. A., Beasley M. A., 2004, *MNRAS*, 355, 1327
- Proctor R. N., Lah P., Forbes D. A., Colless M., Couch W., 2008, *MNRAS*, 386, 1781 (P+08)
- Proctor R. N., Sansom A. A., 2002, *MNRAS*, 333, 517
- Quilis V., Moore B., Bower R., 2000, *Science*, 288, 1617
- Rasmussen J., Ponman T. J., Mulchaey J. S., 2006, *MNRAS*, 370, 453
- Rasmussen J., Ponman T. J., 2007, *MNRAS*, 380, 1554
- Rickes M. G., Pastoriza M. G., Bonatto Ch., 2004, *A&A*, 419, 449
- Sánchez-Blázquez P., et al., 2006, *MNRAS*, 371, 703
- Sánchez-Blázquez P., Forbes D. A., Strader J., Brodie J., Proctor R., 2007, *MNRAS*, 377, 759
- Sansom A. E., Proctor R. N., 1998, *MNRAS*, 297, 953
- Sarzi M., et al., 2006, *MNRAS*, 366, 1151
- Savaglio S., et al., 2005, *ApJ*, 635, 260
- Sivakoff G. R., Sarazin C. L., Carlin J. L., 2004, *ApJ*, 617, 262
- Smith R. J., Lucey J. R., Hudson M. J., 2007, *MNRAS*, 381, 1035
- Smith R. J., et al., 2008a, *MNRAS*, 386, 96
- Smith R. J., Lucey J. R., Hudson M. H., Allanson S. P., Bridges T. J., Hornschemeier A. E., Marzke R. O., Miller N. A., 2008b, arXiv:0810.5558
- Somerville R. S., Primack J. R., 1999, *MNRAS*, 310, 1087
- Spolaor M., Forbes D. A., Proctor R. N., Hau G. K. T., Brough S., 2008, *MNRAS*, 385, 675
- Springel V., et al., 2005, *Nature*, 435, 629
- Terlevich A. I., Forbes D. A., 2002, *MNRAS*, 330, 547
- Temì P., Brighenti F., Mathews W. G., 2007, *ApJ*, 666, 222
- Thomas D., Maraston C., Bender R., 2003, *MNRAS*, 339, 897
- Thomas D., Maraston C., Bender R., Mendes de Oliveira C., 2005, *ApJ*, 621, 673
- Tonry J. L., Dressler A., Blakeslee J. P., Ajhar E. A., Fletcher A. B., Luppino G. A., Metzger M. R., Moore C. B., 2001, *ApJ*, 546, 681
- Toomre A., Toomre J., 1972, *ApJ*, 178, 623
- Tozzi P., Rosati P., Ettori S., Borgani S., Mainieri V., Norman C., 2003, *ApJ*, 593, 705
- Trager S. C., Worthey G., Faber S. M., Burstein D., González J.J., 1998, *ApJS*, 116, 1
- Trager S. C., Faber S. M., Worthey G., González J. J., 2000, *AJ*, 120, 165
- Trager S. C., Faber S. M., Dressler A., 2008, *MNRAS*, 386, 715
- Tremonti C. A., et al., 2004, *ApJ*, 613, 898
- Trentham N., 1994, *Nature*, 372, 157
- van den Bosch F. C., Pasquali A., Yang X., Mo H. J., Weinmann S., McIntosh D. H., Aquino D., 2008, arXiv:0805.0002
- van den Bosch F. C., et al., 2007, *MNRAS*, 376, 841
- van der Marel R. P., Franx M., 1993, *ApJ*, 407, 525
- Woo J., Courteau S., Dekel A., 2008
- Worthey G., Ottaviani D. L., 1997, *ApJS*, 111, 377

## APPENDIX A: INDEX ERRORS

Here we show the error curves for all Lick/IDS indices as derived from AAOmega observations.

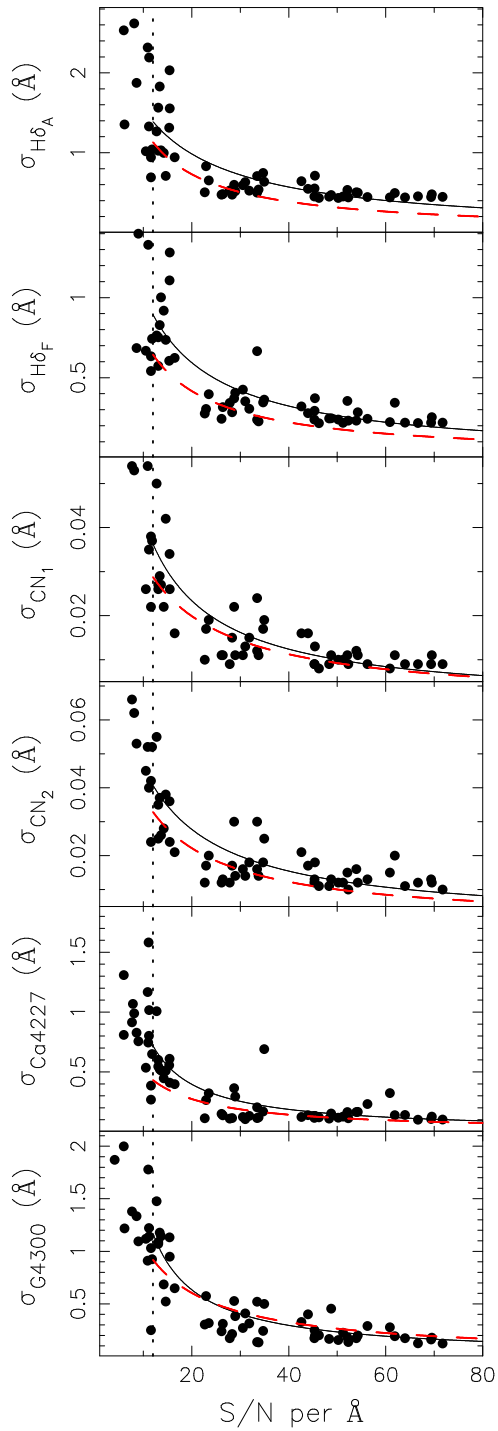


**Figure A1.** Index Error as a function of signal to noise. *Solid* (black) and *dashed* (red) lines represent the best fit hyperbolic functions for these data and the 6dFGS DR1 data of P+08 respectively. The vertical dotted line represents our adopted  $S/N$  cut of 12.

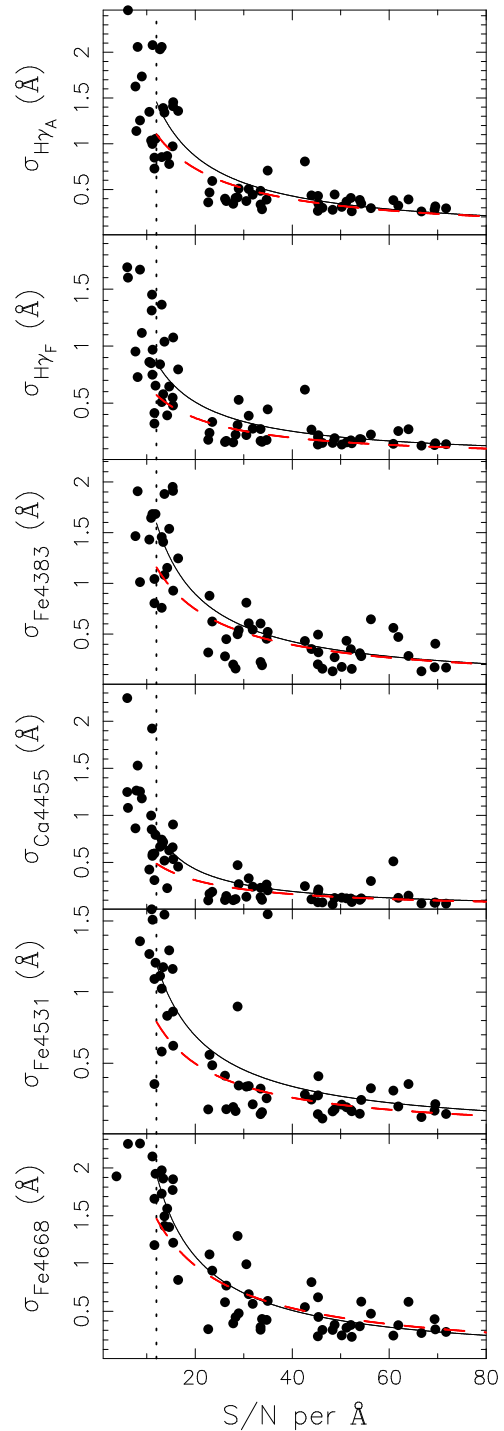


**Figure A2.** Same as Fig. A1

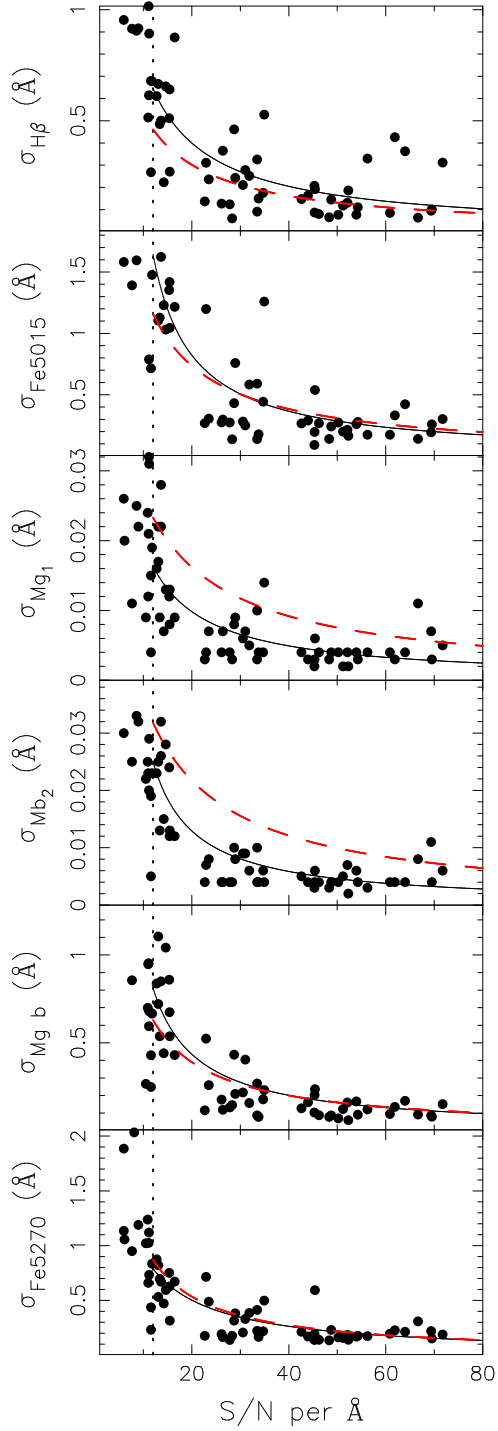


Figure A3. Same as Fig. A1

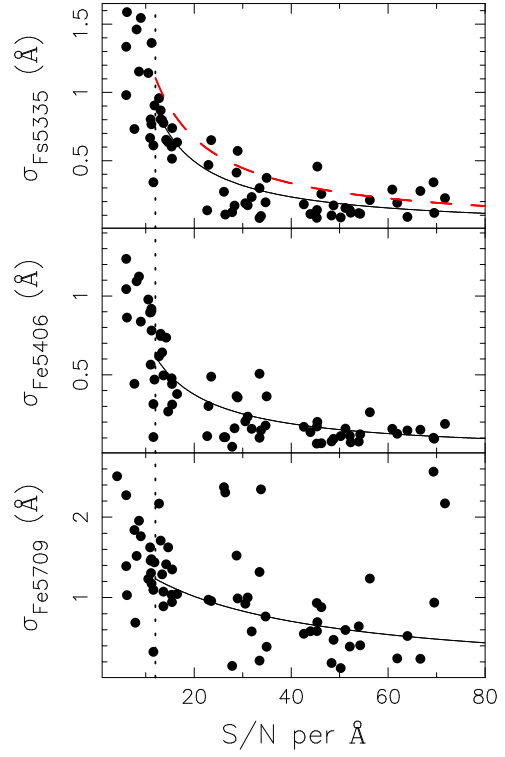


Figure A4. Same as Fig. A1. Fe5406 and Fe5709 indices were not measured in the 6dFGS DR1, so their error curves are omitted.

## **APPENDIX B: STELLAR POPULATION MEASUREMENTS**

Here we include the derived stellar mass, M/L, age, metallicity and  $\alpha$ -element abundance for all 67 galaxies in our spectral sample.

Table B1. Stellar population parameters of NGC 5044 group galaxies. Only those galaxies with S/N &gt; 12 are included (see text.)

Galaxy Identifier	RA (J2000)	DEC (J2000)	log $M_*$	M/L <sub>B</sub>	log age	[Fe/H] (dex)	[ $\alpha$ /Fe] (dex)
(1)	(2)	(3)	(4)	(5)	(6)	(7)	(8)
FS90 003	13 12 26.35	-15 47 52.30	9.3 <sup>+0.1</sup> <sub>-0.1</sub>	0.64 <sup>+0.13</sup> <sub>-0.12</sub>	0.20±0.08	0.03±0.06	0.30±0.08
FS90 005	13 12 54.50	-16 45 57.00	10.5 <sup>+0.1</sup> <sub>-0.1</sub>	3.14 <sup>+0.15</sup> <sub>-0.14</sub>	0.75±0.05	0.33±0.05	0.18±0.05
FS90 009	13 13 5.49	-16 28 41.72	9.9 <sup>+0.1</sup> <sub>-0.1</sub>	2.98 <sup>+0.12</sup> <sub>-0.18</sub>	0.70±0.05	0.25±0.05	0.06±0.05
FS90 011	13 13 6.80	-16 41 0.00	7.8 <sup>+0.1</sup> <sub>-0.1</sub>	1.33 <sup>+0.13</sup> <sub>-0.14</sub>	0.70±0.10	-1.10±0.08	-0.09±0.20
FS90 015	13 13 12.48	-16 7 50.15	9.9 <sup>+0.1</sup> <sub>-0.1</sub>	2.99 <sup>+0.22</sup> <sub>-0.20</sub>	0.82±0.05	-0.05±0.05	0.03±0.05
FS90 017	13 13 28.42	-16 18 52.90	9.0 <sup>+0.1</sup> <sub>-0.1</sub>	1.12 <sup>+0.17</sup> <sub>-0.19</sub>	0.55±0.10	-0.68±0.10	0.03±0.10
FS90 018	13 13 32.24	-17 4 43.40	9.7 <sup>+0.1</sup> <sub>-0.1</sub>	1.49 <sup>+0.18</sup> <sub>-0.13</sub>	0.45±0.07	0.07±0.07	0.03±0.06
FS90 024	13 13 50.96	-16 5 13.70	8.2 <sup>+0.1</sup> <sub>-0.1</sub>	0.78 <sup>+0.15</sup> <sub>-0.10</sub>	0.42±0.10	-1.02±0.10	-0.15±0.19
FS90 027	13 13 54.15	-16 29 27.40	9.9 <sup>+0.1</sup> <sub>-0.1</sub>	2.46 <sup>+0.11</sup> <sub>-0.20</sub>	0.70±0.05	0.05±0.05	0.09±0.05
FS90 029	13 13 56.21	-16 16 24.30	9.3 <sup>+0.0</sup> <sub>-0.0</sub>	2.24 <sup>+0.10</sup> <sub>-0.06</sub>	0.72±0.05	-0.20±0.05	0.00±0.07
FS90 030	13 13 59.52	-16 23 3.80	9.3 <sup>+0.0</sup> <sub>-0.0</sub>	3.00 <sup>+0.22</sup> <sub>-0.21</sub>	1.07±0.05	-0.62±0.05	0.15±0.08
FS90 031	13 14 0.47	-16 0 44.20	8.4 <sup>+0.1</sup> <sub>-0.1</sub>	1.01 <sup>+0.11</sup> <sub>-0.03</sub>	0.70±0.08	-1.25±0.06	0.40±0.26
FS90 032	13 14 3.22	-16 7 23.20	10.3 <sup>+0.1</sup> <sub>-0.1</sub>	5.10 <sup>+0.38</sup> <sub>-0.35</sub>	1.07±0.05	0.15±0.05	0.24±0.05
FS90 034	13 14 7.40	-16 25 35.80	9.0 <sup>+0.0</sup> <sub>-0.0</sub>	3.00 <sup>+0.14</sup> <sub>-0.14</sub>	1.02±0.05	-0.57±0.05	0.00±0.07
FS90 038	13 14 13.24	-16 19 29.00	8.7 <sup>+0.0</sup> <sub>-0.0</sub>	3.43 <sup>+0.22</sup> <sub>-0.21</sub>	1.02±0.05	-0.30±0.05	0.12±0.06
FS90 040	13 14 0.30	-16 47 10.00	8.9 <sup>+0.2</sup> <sub>-0.1</sub>	1.38 <sup>+0.29</sup> <sub>-0.20</sub>	0.68±0.16	-0.95±0.12	-0.18±0.30
FS90 042	13 14 17.36	-16 26 19.50	9.3 <sup>+0.0</sup> <sub>-0.0</sub>	2.81 <sup>+0.15</sup> <sub>-0.14</sub>	0.97±0.05	-0.45±0.05	0.09±0.06
FS90 049	13 14 31.23	-16 22 47.60	8.6 <sup>+0.1</sup> <sub>-0.1</sub>	0.69 <sup>+0.11</sup> <sub>-0.15</sub>	0.38±0.13	-1.20±0.15	-0.18±0.17
FS90 050	13 14 34.86	-16 29 28.90	8.8 <sup>+0.0</sup> <sub>-0.1</sub>	0.84 <sup>+0.06</sup> <sub>-0.09</sub>	0.38±0.08	-0.42±0.08	0.12±0.06
FS90 051	13 14 35.84	-16 34 50.40	8.8 <sup>+0.0</sup> <sub>-0.1</sub>	1.65 <sup>+0.08</sup> <sub>-0.22</sub>	0.57±0.06	-0.28±0.08	0.03±0.07
FS90 053	13 14 39.22	-15 50 36.00	8.3 <sup>+0.1</sup> <sub>-0.0</sub>	0.74 <sup>+0.09</sup> <sub>-0.06</sub>	0.45±0.07	-1.18±0.08	0.06±0.10
FS90 054	13 14 39.40	-16 10 4.00	9.0 <sup>+0.1</sup> <sub>-0.1</sub>	2.89 <sup>+0.35</sup> <sub>-0.38</sub>	1.07±0.10	-0.70±0.08	0.18±0.20
FS90 058	13 14 43.61	-15 51 34.40	7.7 <sup>+0.1</sup> <sub>-0.1</sub>	1.00 <sup>+0.28</sup> <sub>-0.26</sub>	0.60±0.20	-1.07±0.16	0.15±0.25
FS90 063	13 14 49.82	-16 58 24.20	9.7 <sup>+0.0</sup> <sub>-0.0</sub>	2.58 <sup>+0.19</sup> <sub>-0.14</sub>	0.82±0.05	-0.17±0.05	0.09±0.06
FS90 064	13 14 49.23	-16 29 33.69	9.7 <sup>+0.1</sup> <sub>-0.1</sub>	1.06 <sup>+0.10</sup> <sub>-0.11</sub>	0.30±0.05	0.17±0.06	0.12±0.05
FS90 068	13 14 59.37	-16 35 25.10	10.6 <sup>+0.1</sup> <sub>-0.1</sub>	3.44 <sup>+0.24</sup> <sub>-0.21</sub>	0.88±0.05	0.17±0.05	0.21±0.05
FS90 072	13 15 2.13	-15 57 6.50	9.3 <sup>+0.1</sup> <sub>-0.1</sub>	0.40 <sup>+0.02</sup> <sub>-0.04</sub>	0.00±0.06	-0.12±0.05	0.06±0.06
FS90 075	13 15 4.08	-16 23 40.20	9.1 <sup>+0.0</sup> <sub>-0.0</sub>	2.18 <sup>+0.11</sup> <sub>-0.04</sub>	0.75±0.05	-0.17±0.05	0.12±0.06
FS90 078	13 15 10.54	-16 14 19.55	9.8 <sup>+0.1</sup> <sub>-0.1</sub>	3.52 <sup>+0.24</sup> <sub>-0.24</sub>	1.02±0.05	-0.12±0.05	0.27±0.06
FS90 079	13 15 12.71	-16 29 57.10	9.2 <sup>+0.0</sup> <sub>-0.0</sub>	3.21 <sup>+0.22</sup> <sub>-0.15</sub>	0.97±0.05	-0.28±0.05	0.09±0.06
FS90 081	13 15 14.30	-15 50 59.00	8.0 <sup>+0.2</sup> <sub>-0.2</sub>	2.55 <sup>+0.56</sup> <sub>-0.54</sub>	1.07±0.16	-0.97±0.09	0.21±0.23
FS90 082	13 15 17.57	-16 29 10.19	9.4 <sup>+0.1</sup> <sub>-0.0</sub>	1.37 <sup>+0.15</sup> <sub>-0.12</sub>	0.45±0.07	-0.05±0.07	0.03±0.06
FS90 084	13 15 23.97	-16 23 7.90	11.3 <sup>+0.1</sup> <sub>-0.1</sub>	6.85 <sup>+0.49</sup> <sub>-0.41</sub>	1.18±0.05	0.25±0.05	0.24±0.05
FS90 094	13 15 32.04	-16 28 51.10	9.5 <sup>+0.0</sup> <sub>-0.0</sub>	3.63 <sup>+0.20</sup> <sub>-0.20</sub>	1.00±0.05	-0.23±0.05	0.06±0.06
FS90 095	13 15 32.40	-16 38 12.00	8.3 <sup>+0.1</sup> <sub>-0.1</sub>	2.40 <sup>+0.11</sup> <sub>-0.14</sub>	1.07±0.08	-1.02±0.05	0.30±0.20
FS90 096	13 15 32.70	-16 50 35.00	7.9 <sup>+0.2</sup> <sub>-0.2</sub>	1.16 <sup>+0.37</sup> <sub>-0.27</sub>	0.80±0.16	-1.50±0.12	0.56±0.32
FS90 100	13 15 45.12	-16 19 36.63	10.2 <sup>+0.1</sup> <sub>-0.1</sub>	5.01 <sup>+0.38</sup> <sub>-0.35</sub>	1.07±0.05	0.10±0.05	0.21±0.05
FS90 102	13 15 48.52	-16 31 8.00	10.0 <sup>+0.1</sup> <sub>-0.1</sub>	1.59 <sup>+0.08</sup> <sub>-0.19</sub>	0.60±0.06	-0.07±0.07	0.34±0.07
FS90 107	13 15 59.30	-16 23 49.80	10.3 <sup>+0.1</sup> <sub>-0.1</sub>	3.73 <sup>+0.30</sup> <sub>-0.26</sub>	0.93±0.05	0.20±0.05	0.27±0.05
FS90 108	13 15 59.90	-16 10 32.00	8.6 <sup>+0.1</sup> <sub>-0.1</sub>	2.78 <sup>+0.32</sup> <sub>-0.33</sub>	1.07±0.09	-0.85±0.05	0.12±0.14
FS90 117	13 16 23.11	-16 8 11.35	9.4 <sup>+0.0</sup> <sub>-0.0</sub>	2.83 <sup>+0.17</sup> <sub>-0.15</sub>	0.95±0.05	-0.30±0.05	0.18±0.06
FS90 123	13 16 35.62	-16 26 5.70	8.5 <sup>+0.1</sup> <sub>-0.1</sub>	3.45 <sup>+0.24</sup> <sub>-0.22</sub>	1.15±0.06	-0.68±0.05	0.09±0.10
FS90 127	13 16 39.40	-16 57 3.00	8.4 <sup>+0.1</sup> <sub>-0.1</sub>	3.41 <sup>+0.25</sup> <sub>-0.22</sub>	1.02±0.07	-0.70±0.06	-0.30±0.10
FS90 133	13 16 55.43	-16 26 32.20	7.7 <sup>+0.1</sup> <sub>-0.1</sub>	0.82 <sup>+0.09</sup> <sub>-0.10</sub>	0.53±0.09	-0.93±0.08	0.46±0.17
FS90 134	13 16 56.23	-16 35 34.70	9.1 <sup>+0.1</sup> <sub>-0.1</sub>	0.75 <sup>+0.08</sup> <sub>-0.06</sub>	0.47±0.07	-1.25±0.08	0.06±0.13
FS90 135	13 16 54.40	-16 3 18.00	8.2 <sup>+0.1</sup> <sub>-0.1</sub>	2.47 <sup>+0.18</sup> <sub>-0.21</sub>	1.07±0.09	-0.85±0.06	0.42±0.23
FS90 137	13 16 58.49	-16 38 5.50	10.5 <sup>+0.1</sup> <sub>-0.1</sub>	0.68 <sup>+0.10</sup> <sub>-0.14</sub>	0.12±0.07	0.10±0.06	0.00±0.06
FS90 138	13 17 3.10	-16 35 39.00	8.0 <sup>+0.1</sup> <sub>-0.1</sub>	2.04 <sup>+0.17</sup> <sub>-0.21</sub>	1.02±0.10	-1.02±0.05	0.46±0.23
FS90 144	13 17 10.79	-16 13 46.74	9.9 <sup>+0.1</sup> <sub>-0.1</sub>	3.49 <sup>+0.23</sup> <sub>-0.22</sub>	1.05±0.05	-0.17±0.05	0.30±0.05
FS90 153	13 17 36.38	-16 32 25.40	9.5 <sup>+0.0</sup> <sub>-0.0</sub>	2.60 <sup>+0.14</sup> <sub>-0.15</sub>	0.88±0.05	-0.33±0.05	0.06±0.08
FS90 158	13 18 9.04	-16 58 15.60	8.9 <sup>+0.1</sup> <sub>-0.1</sub>	2.92 <sup>+0.19</sup> <sub>-0.25</sub>	1.10±0.06	-0.97±0.05	0.00±0.11
FS90 161	13 18 17.80	-16 38 25.00	8.0 <sup>+0.2</sup> <sub>-0.2</sub>	1.91 <sup>+0.77</sup> <sub>-0.40</sub>	1.02±0.20	-1.20±0.07	0.42±0.37
2MASXJ13102493-1655578	13 10 24.96	-16 55 57.50	9.8 <sup>+0.1</sup> <sub>-0.2</sub>	1.41 <sup>+0.32</sup> <sub>-0.29</sub>	0.70±0.15	-0.57±0.13	0.32±0.15
2MASXJ13114576-1915421	13 11 45.77	-19 15 42.30	...	4.11 <sup>+0.29</sup> <sub>-0.30</sub>	1.00±0.06	-0.05±0.05	0.09±0.07
2MASXJ13115849-1644541	13 11 58.49	-16 44 54.10	9.6 <sup>+0.1</sup> <sub>-0.1</sub>	2.98 <sup>+0.12</sup> <sub>-0.12</sub>	1.00±0.06	-0.53±0.05	0.00±0.12
2MASXJ13125449-1645571 (FS90 005)	13 12 54.50	-16 45 57.00	10.6 <sup>+0.1</sup> <sub>-0.1</sub>	4.07 <sup>+0.25</sup> <sub>-0.26</sub>	1.02±0.06	-0.10±0.05	0.12±0.07

Table B1—Continued

Galaxy Identifier	RA (J2000)	DEC (J2000)	$\log M_*$	M/L <sub>B</sub>	log age	[Fe/H] (dex)	[ $\alpha$ /Fe] (dex)
(1)	(2)	(3)	(4)	(5)	(6)	(7)	(8)
2MASXJ13130549-1628411 (FS90 009)	13 13 5.49	-16 28 41.72	$9.9^{+0.1}_{-0.1}$	$3.23^{+0.28}_{-0.30}$	$0.85 \pm 0.08$	$-0.07 \pm 0.06$	$-0.03 \pm 0.10$
2MASXJ13143041-1732009	13 14 30.42	-17 32 0.90	$9.4^{+0.1}_{-0.1}$	$1.83^{+0.18}_{-0.12}$	$0.90 \pm 0.07$	$-1.40 \pm 0.05$	$-0.30 \pm 0.14$
2MASXJ13143485-1629289 (FS90 050)	13 14 34.86	-16 29 28.90	$8.5^{+0.5}_{-0.2}$	$0.41^{+0.47}_{-0.13}$	$0.10 \pm 0.29$	$-0.57 \pm 0.20$	$-0.30 \pm 0.12$
2MASXJ13150409-1623391 (FS90 075)	13 15 4.08	-16 23 40.20	$9.4^{+0.1}_{-0.1}$	$3.83^{+0.29}_{-0.27}$	$0.97 \pm 0.07$	$-0.35 \pm 0.05$	$-0.21 \pm 0.09$
2MASXJ13153203-1628509 (FS90 094)	13 15 32.04	-16 28 51.10	$9.1^{+0.2}_{-0.2}$	$1.64^{+0.38}_{-0.34}$	$0.45 \pm 0.14$	$0.00 \pm 0.14$	$-0.18 \pm 0.12$
2MASXJ13164875-1620397	13 16 48.75	-16 20 39.70	$9.5^{+0.1}_{-0.1}$	$2.93^{+0.22}_{-0.25}$	$1.07 \pm 0.07$	$-0.75 \pm 0.05$	$0.09 \pm 0.16$
2MASXJ13165533-1756417	13 16 55.35	-17 56 42.00	$9.5^{+0.1}_{-0.1}$	$2.41^{+0.28}_{-0.28}$	$0.97 \pm 0.08$	$-0.88 \pm 0.05$	$-0.06 \pm 0.14$
2MASXJ13165624-1635347 (FS90 134)	13 16 56.23	-16 35 34.70	$9.6^{+0.1}_{-0.1}$	$2.50^{+0.22}_{-0.24}$	$1.07 \pm 0.09$	$-1.50 \pm 0.06$	$-0.30 \pm 0.18$
2MASXJ13171239-1715162	13 17 12.40	-17 15 16.10	$9.7^{+0.1}_{-0.1}$	$1.34^{+0.18}_{-0.13}$	$0.62 \pm 0.10$	$-0.78 \pm 0.08$	$-0.15 \pm 0.11$
2MASXJ13184125-1904476	13 18 41.26	-19 4 47.70	$8.9^{+0.2}_{-0.2}$	$0.39^{+0.18}_{-0.12}$	$-0.05 \pm 0.18$	$-0.10 \pm 0.07$	$-0.06 \pm 0.15$
2MASXJ13185909-1835167	13 18 59.09	-18 35 16.70	$10.1^{+0.1}_{-0.1}$	$3.21^{+0.24}_{-0.25}$	$0.85 \pm 0.06$	$0.03 \pm 0.05$	$0.09 \pm 0.07$